



# Changes in silicate utilisation and upwelling intensity off Peru since the Last Glacial Maximum – insights from silicon and neodymium isotopes

C. Ehlert\*, P. Grasse, M. Frank

GEOMAR Helmholtz Centre for Ocean Research Kiel, Germany

## ARTICLE INFO

### Article history:

Received 6 November 2012

Received in revised form

11 April 2013

Accepted 19 April 2013

Available online

### Keywords:

Silicate utilisation

Silicon isotopes

Diatoms

Neodymium isotopes

Peruvian upwelling

Upwelling intensity

ENSO intensity

## ABSTRACT

We combine the stable silicon isotope composition ( $\delta^{30}\text{Si}$ ) of diatoms and the radiogenic neodymium isotope compositions ( $\epsilon_{\text{Nd}}$ ) of past seawater extracted from the authigenic fraction of the sediments (Mn–Fe coatings of particles and benthic foraminifers), as well as the radiogenic isotope compositions (Nd, Sr) of the detrital material itself to reconstruct silicic acid utilisation, water mass mixing, and upwelling intensity from the same marine sediments in the Peruvian upwelling region during the past 20,000 years. Additionally, the sedimentary signals were compared to the water column isotope compositions.

Along the Peruvian shelf, the dissolved  $\epsilon_{\text{Nd}}$  in the water column ranges from  $-5.7$  to  $+0.6$ . The corresponding  $\epsilon_{\text{Nd}}$  signatures of the coatings and the benthic foraminifers of the surface sediments range from  $-4.5$  to  $+1.8$  and from  $-2.5$  to  $+2.2$ , respectively. The detrital  $\epsilon_{\text{Nd}}$  ( $^{87}\text{Sr}/^{86}\text{Sr}$ ) signatures range from  $-6.3$  to  $0$  ( $0.70508$ – $0.71049$ ). All phases show a trend from more radiogenic  $\epsilon_{\text{Nd}}$  values in the north towards less radiogenic values in the south broadly reflecting local weathering inputs and hinterland geology.

The  $\epsilon_{\text{Nd}}$  signatures of the coatings extracted from sediment core SO147-106KL located in the present day centre of coastal upwelling near  $12^\circ\text{S}$  have been essentially constant ( $-1.5$ ) throughout the past 20,000 years, while the detrital  $\epsilon_{\text{Nd}}$  ( $^{87}\text{Sr}/^{86}\text{Sr}$ ) varied between values of  $-0.7$  ( $0.70620$ ) during the Last Glacial and  $-4.5$  ( $0.70849$ ) during the late Holocene reflecting changes in the origin of the sediment and current transport from a more northerly towards a more southerly source and from overall stronger to weaker upwelling. The  $\delta^{30}\text{Si}$  signature of both total biogenic opal ( $\delta^{30}\text{Si}_{\text{opal}}$ ) and of hand-picked diatoms ( $\delta^{30}\text{Si}_{\text{diatom}}$ ) ranged from  $+0.3\text{‰}$  (Last Glacial) to  $+1.4\text{‰}$  (late Holocene) confirming large variations in upwelling intensity driving silicic acid utilisation by diatoms. Our combined bSiO<sub>2</sub> MAR,  $\delta^{30}\text{Si}_{\text{opal}}$  and detrital radiogenic isotope results demonstrate that the strongest El Niño–Southern Oscillation conditions off Peru of the past 20 ka have prevailed during the past 5 ka.

© 2013 Elsevier Ltd. All rights reserved.

## 1. Introduction

The Peruvian continental margin is characterised by one of the most pronounced Oxygen Minimum Zones (OMZs) in the world's ocean (e.g., Karstensen et al., 2008; Fuenzalida et al., 2009). The effects of oxygen-dependent nutrient cycling (e.g. for nitrogen, phosphorus and iron) in this region are distributed via currents and exert a far-reaching influence, partly affecting the global ocean. Past oxygen variability in the Peru region has primarily been considered a function of upwelling intensity driven by an interplay of major

currents with trade winds and the El Niño–Southern Oscillation (ENSO) (Brink et al., 1983) and surface water bioproductivity (e.g. De Vries and Schrader, 1981; Thiede and Suess, 1983; Rein et al., 2004, 2005). ENSO is a key component of the tropical climate system (Fedorov and Philander, 2000). Its intensity has varied strongly in the past over centennial to glacial–interglacial time-scales (Rein et al., 2005; Agnihotri et al., 2008; Koutavas and Joanides, 2012). The Peruvian region is particularly influenced by ENSO, which exerts control on circulation, biological productivity and ecosystem structure (Pennington et al., 2006). During El Niño events the Pacific region has experienced a mean southward shift of the ITCZ (Fedorov and Philander, 2000). Consequences are weaker trade winds and reduced coastal upwelling of nutrient-rich subsurface waters along the Peruvian shelf causing higher sea surface temperatures, a reduction in primary productivity (Barber and Chavez, 1983; Fiedler, 2002) and higher precipitation in the Andean hinterland (Bendix, 2000; Baker et al., 2001).

\* Corresponding author. Now at: Max Planck Research Group for Marine Isotope Geochemistry, Institute for Chemistry and Biology of the Marine Environment (ICBM), University of Oldenburg, Carl-von-Ossietzky-Str. 9–11, 26129 Oldenburg, Germany. Tel.: +49 441 798 3359.

E-mail address: [cehlert@mpi-bremen.de](mailto:cehlert@mpi-bremen.de) (C. Ehlert).

### 1.1. Nutrient cycling, utilisation and silicon isotopes

In the Peruvian upwelling system primary productivity is dominated by diatoms (Estrada and Blasco, 1985; Abrantes et al., 2007) which build their opaline frustules from dissolved silicic acid ( $\text{Si}(\text{OH})_4$ ) (Tréguer et al., 1995). The nutrients feeding the productivity are mainly supplied via upwelling of the southward flowing subsurface waters of the Peru–Chile Undercurrent (PCUC) (Fig. 1) (Brink et al., 1983). This current is partly fed by the eastward flowing oxygen rich waters of the Equatorial Undercurrent (EUC) (Lukas, 1986; Penven et al., 2005; Kessler, 2006) originating from the central Pacific (Brink et al., 1983; Toggweiler et al., 1991) as a mixture of waters of southern and northern Pacific origin (Dugdale et al., 2002). Also, water masses from the south, such as the Subantarctic Mode Water (SAMW), the Peru–Chile Current (PCC) and the Peru Coastal Current (PCoastalC) affect nutrient transport and upwelling intensity (Toggweiler et al., 1991; Sarmiento et al., 2004). As a result, past changes in  $\text{Si}(\text{OH})_4$  concentrations in the high latitudes have also been invoked to affect tropical  $\text{Si}(\text{OH})_4$  supply and diatom productivity, as proposed by the silicic acid leakage hypothesis (SALH) (e.g., Nozaki and Yamamoto, 2001; Brzezinski et al., 2002; Matsumoto and Sarmiento, 2008), and thus ultimately also influenced extent and strength of the OMZ.

The stable silicon isotopic composition (expressed as  $\delta^{30}\text{Si}$ , which is the measured  $^{30}\text{Si}/^{28}\text{Si}$ , normalised to that of the international standard NBS28, multiplied by 1000) of the diatom frustules ( $\delta^{30}\text{Si}_{\text{opal}}$ ) is a powerful tool to investigate changes of  $\text{Si}(\text{OH})_4$  utilisation, as well as nutrient dynamics and productivity in the present and past ocean (e.g., De La Rocha et al., 1998; Brzezinski et al., 2002; Reynolds et al., 2008; Pichevin et al., 2009). Diatoms preferentially incorporate the lighter  $^{28}\text{Si}$  during opal formation, which leaves the residual seawater enriched in the heavy isotopes. Earlier studies found the fractionation factor  $\epsilon$  between seawater and diatoms accompanying this process to be species-independent near  $-1.1\text{‰}$  (De La Rocha et al., 1997; Milligan et al., 2004; Varela et al., 2004; Reynolds et al., 2006; Beucher et al., 2008). However, recent culturing experiments on diatom species, e.g. *Chaetoceros brevis*, indicate that  $\epsilon$  can be species dependent and encompasses a large range of  $-0.5$  to  $-2.1\text{‰}$  (Sutton et al., 2013).

### 1.2. Silicon isotope composition in surface sediments off Peru

The silicon isotope composition of the surface waters in the Eastern Equatorial Pacific (EEP) can be extracted from diatoms from the surface sediments and is mainly controlled by  $\text{Si}(\text{OH})_4$  utilisation

by diatoms and by upwelling intensity (Ehlert et al., 2012). Diatom primary productivity in the surface waters along the Peruvian shelf region is highest within the main upwelling region between  $5^\circ\text{S}$  and  $15^\circ\text{S}$ . Today, under conditions of strong upwelling, the rates of re-supply of the surface waters with isotopically less fractionated  $\text{Si}(\text{OH})_4$  from the upwelled subsurface waters are high and thus the degree of surface water  $\text{Si}(\text{OH})_4$  utilisation by the diatoms is only 50–70%. This is reflected by low  $\delta^{30}\text{Si}$  both in surface waters ( $\sim +1.7\text{‰}$ ) and correspondingly in the diatoms ( $\sim +0.6\text{‰}$ ) produced from these waters. Within the main upwelling region, the  $\text{Si}(\text{OH})_4$  utilisation and Si isotope distribution can be explained by steady state-type fractionation. In contrast, under weaker upwelling conditions north of  $5^\circ\text{S}$  and partly south of  $15^\circ\text{S}$  re-supply of  $\text{Si}(\text{OH})_4$  is less efficient and the diatoms utilise the available  $\text{Si}(\text{OH})_4$  more completely resulting in utilisation near 90% reflected by higher Si isotope ratios in both the surface waters ( $\sim +2.8\text{‰}$ ) and the diatoms ( $\sim +1.6\text{‰}$ ) that grew from them. Both surface waters and diatoms indicate that in these areas the fractionation of Si isotopes rather follows a Rayleigh-type model. However, the varying upwelling conditions cause differences in the dominating diatom assemblages and the importance of seasonality effects. In the central, upwelling-dominated area, the diatom assemblages are dominated by *Chaetoceros* sp. (Abrantes et al., 2007), which are indicative of coastal upwelling, high-nutrient conditions. Further north and south the influence of seasonality (and therefore upwelling intensity and nutrient supply) becomes larger, which is reflected by mixed assemblages of diatoms indicating high-nutrient levels and others including larger diatom species such as *Coscinodiscus* sp. growing under weaker upwelling (lower nutrient) conditions during austral summer (De Vries and Schrader, 1981; Brodie and Kemp, 1994).

Additionally, the distribution of dissolved  $\delta^{30}\text{Si}$  signatures and  $\text{Si}(\text{OH})_4$  concentrations in the water column documents the strong influence of water mass mixing on both the dissolved Si isotope compositions at a particular location and their vertical and horizontal gradients (Ehlert et al., 2012). Therefore, the  $\delta^{30}\text{Si}$  signatures of water and diatom opal are not only controlled by  $\text{Si}(\text{OH})_4$  utilisation but are also strongly influenced by upwelling intensity and water mass advection (Reynolds et al., 2006; Beucher et al., 2011; De Souza et al., 2012), two processes that are difficult to disentangle in the paleo-record.

### 1.3. Radiogenic neodymium and strontium isotopes

Information on past changes in water mass advection and vertical mixing can be gained from radiogenic Nd isotopes. Water

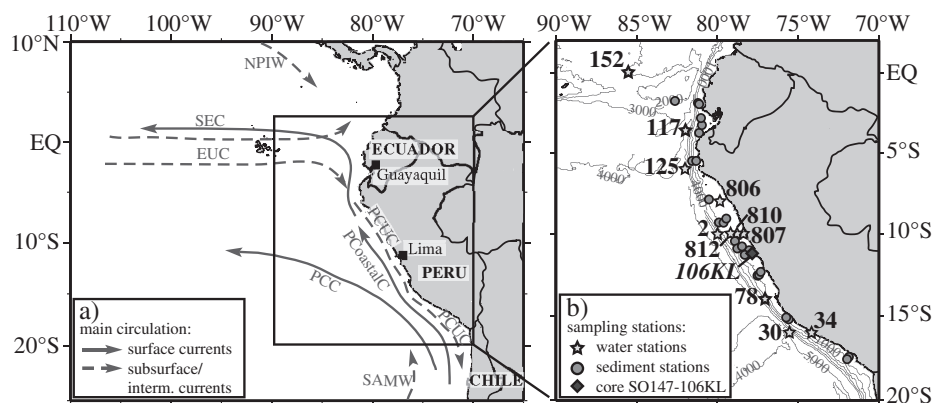


**Fig. 1.** a) Schematic ocean circulation and main currents in the EEP: Surface currents (solid lines): (n)SEC (northern) South Equatorial Current, PCC Peru–Chile Current, PCoastalC Peru Coastal Current and intermediate currents (dashed lines): EUC Equatorial Undercurrent, PCUC Peru–Chile Undercurrent, SAMW Subantarctic Mode Waters, NPIW North Pacific Intermediate Water (after Penven et al., 2005; Kessler, 2006; Bostock et al., 2010; and ADCP data from Czeschel et al., 2011). b) Station map for water column stations (light grey stars with station numbers), surface sediments (grey dots) and the location of core SO147-106KL (black diamond). The bathymetry is given for 0–5000 m water depth in 1000 m increments.

masses acquire their Nd isotope composition (expressed as  $\epsilon_{\text{Nd}}$ , which corresponds to the measured  $^{143}\text{Nd}/^{144}\text{Nd}$ , normalised to the Chondritic Uniform Reservoir CHUR (0.512638), multiplied by 10,000) in their source regions through weathering of continental rocks with distinct isotopic signatures supplied to the oceans via rivers, eolian inputs or through shelf exchange processes (e.g. Frank, 2002; Lacan and Jeandel, 2005). In the EEP three main endmembers dominate the Nd isotope signal. Water masses of Southern Ocean origin have less radiogenic signatures between  $-5$  and  $-9$  (Piepgras and Wasserburg, 1982; Stichel et al., 2012) whereas more radiogenic signatures of up to  $-1.6$  reflect contributions from the central Pacific on the one hand (Lacan and Jeandel, 2001; Grasse et al., 2012) and from the northern Pacific on the other (Piepgras and Jacobsen, 1988; Amakawa et al., 2009). Past bottom water Nd isotopic compositions are preserved either in early diagenetic, authigenic ferromanganese oxyhydroxide coatings of the sediment particles ( $\epsilon_{\text{Nd}_{\text{coating}}}$ ) that can be extracted from bulk sediments (Rutberg et al., 2000; Gutjahr et al., 2007) or from the carbonate fraction of benthic foraminifers ( $\epsilon_{\text{Nd}_{\text{foram}}}$ ) (Klevenz et al., 2008). In addition, lithogenic particles in the sediments delivered to the shelf via weathering of continental source rocks of different origin and age, which have subsequently been transported by currents, in particular their fine fractions, have distinct radiogenic isotope signatures ( $\epsilon_{\text{Nd}_{\text{detritus}}}$ ,  $^{87}\text{Sr}/^{86}\text{Sr}_{\text{detritus}}$ ), which can be used to trace their source areas (Goldstein et al., 1984; Dia et al., 1992; Fagel et al., 2004). Changes in the detrital signal have thus been closely related to climatic changes causing variations in current strength and transport pathways of the particles from their respective source areas (Grousset et al., 1988; Fagel et al., 2004; Ehlert et al., 2011; Stumpf et al., 2011). Periods of weaker upwelling (e.g. prolonged El Niño-like phases) resulted in a diminished nutrient supply to the euphotic zone (Barber and Chavez, 1983). Subsurface waters were replaced by more oligotrophic surface waters and in particular the flowpath of the northward flowing Peru Coastal Current (PCoastalC) was shifted more closely to the coast (Huyer et al., 1987; Fiedler and Talley, 2006), resulting in a general decrease of primary productivity and a change in phytoplankton assemblages (Feldman et al., 1984; Chavez, 2005). These drastic changes are expected to be reflected in the sedimentary Si, Nd and Sr isotope records and will allow reconstruction of the controlling factors of upwelling intensity and oxygen levels in the OMZ in the past 20 ka.

This study for the first time aims to reconstruct  $\text{Si}(\text{OH})_4$  utilisation and upwelling intensity, as well as water mass mixing by means of combined Si isotope compositions in diatoms and Nd isotope compositions of past seawater extracted from authigenic fractions (Mn–Fe coatings of particles and benthic foraminifers), as well as Nd and Sr isotope compositions of detrital material at the centre of coastal upwelling on the Peruvian shelf during the past 20,000 years. Prior to the downcore analyses, the Nd isotope compositions of the seawater-derived, authigenic and detrital fractions of the surface sediments between the equator and  $18^\circ\text{S}$  were compared to the Nd isotope compositions of the overlying water column in order to achieve a detailed picture of the present day distribution.

## 2. Material and methods

### 2.1. Core location, age model and sampling

Water and surface sediment samples for Si and Nd isotope analyses were taken onboard RV Meteor during cruises M77/1 to 4 along the Ecuadorian and Peruvian shelf between  $0^\circ\text{S}$  and  $18^\circ\text{S}$  at water depths between 114 m and 2600 m in the years 2008/09 (Fig. 1, Tables 1 and 2). Nd and Si isotope measurements for the reconstruction of past conditions were conducted on core SO147-106KL, which was recovered during RV Sonne cruise SO147 along

the central Peruvian shelf in 184 m water depth at  $12^\circ 03' \text{S}$ ,  $77^\circ 39.8' \text{W}$  in 2000 (Fig. 1, Table 3) (Dullo et al., 2000). The age determination of the upper 11 m of the core is based on radioactive caesium ( $^{137}\text{Cs}$ ) and lead ( $^{210}\text{Pb}$ ) profiling in its youngest part and 45 AMS  $^{14}\text{C}$  measurements of the bulk organic carbon fraction (Rein et al., 2004, 2005). The oldest radiocarbon age is 19.6 ka BP and the age model of the core is based on linearly interpolated ages between the calibrated radiocarbon ages (all ages in the following are given in ka B.P.).

### 2.2. Biogenic opal and silicon isotope analyses

The  $\text{bSiO}_2$  content in the sediment (Wolf, 2002) was measured following the sodium carbonate sequential leaching methods described by DeMaster (1981) and Müller and Schneider (1993). For silicon isotope measurements diatoms were extracted from the sediment in two different ways. For the size fraction 11–32  $\mu\text{m}$  the procedures described by Morley et al. (2004) were applied, for which approximately 300 mg sediment were treated with 30%  $\text{H}_2\text{O}_2$  and 35% HCl to remove the organic and carbonate fractions. Afterwards the sediment was wet-sieved to separate the 11–32  $\mu\text{m}$  fraction. In a third step a heavy-liquid solution (sodium-polytungstate, 2.1–2.2 g/mL) was applied in several steps to separate diatoms from detrital lithic silicate material. The surface sediment calibration study for  $\delta^{30}\text{Si}$  indicated that samples with low  $\text{bSiO}_2$  content are easily biased by other siliceous material such as sponge spicules, which can significantly influence the measured Si isotope ratios (Ehlert et al., 2012). Therefore, all samples were screened carefully under the microscope to verify their purity from the detrital (clay) fraction and from other opal phases such as sponge spicules prior to dissolution and only pure diatom samples were further treated. In an alternative procedure large diatoms were hand-picked from the size fraction 125–250  $\mu\text{m}$  (Ehlert et al., 2012). The samples were then transferred into Teflon vials and dissolved in 1 mL 0.1 M NaOH at  $130^\circ\text{C}$  for ca 12 h. After cooling the samples were centrifuged to separate any residual material and the supernatant was transferred into a new Teflon vial. 200  $\mu\text{L}$  concentrated  $\text{H}_2\text{O}_2$  (Suprapur<sup>®</sup>) was added to each sample, which was then dried and redissolved in 1 mL 0.1 M NaOH at  $130^\circ\text{C}$  for a few hours. The sample solution was then diluted with 4 mL MQ water and neutralised with 0.1 mL 1 M HCl (Reynolds et al., 2008). Si concentrations of the dissolved diatom samples were measured colourimetrically using a photospectrometer (Hansen and Koroleff, 1999). All sample solutions were chromatographically purified with 1 mL pre-cleaned AG50W-X8 cation exchange resin (BioRad<sup>®</sup>, mesh 200–400) following the method described by Georg et al. (2006) as modified by De Souza et al. (2012). Si isotope ratios were measured on a NuPlasma HR MC-ICPMS (Nu Instruments) at GEOMAR, equipped with an adjustable source-defining slit set to medium resolution to ensure separation of the  $^{30}\text{Si}$  peak and molecular interferences. The measurements were carried out applying a standard-sample bracketing method (Albarède et al., 2004). All solutions were measured at a Si concentration of 14–21  $\mu\text{mol}/\text{kg}$  depending on the sensitivity of the instrument on the respective measurement day and were introduced into the plasma via a Cetac Aridus II desolvating nebulizer system equipped with a PFA nebulizer yielding a 60–80  $\mu\text{L}/\text{min}$  uptake rate. Repeated measurements of the reference materials IRMM018 and Big Batch gave average  $\delta^{30}\text{Si}$  values of  $-1.56 \pm 0.17\text{‰}$  ( $2\sigma_{\text{sd}}$ ) and  $-10.81 \pm 0.17\text{‰}$  ( $2\sigma_{\text{sd}}$ ), respectively, which are in agreement with values obtained by other laboratories (Reynolds et al., 2007). Samples were measured on at least two separate days and three to five times within a day session, which generally resulted in uncertainties between 0.07 and 0.30‰ during a particular session ( $2\sigma_{\text{sd}}$ ) (Table 3). Replicate measurements of an in-house diatom matrix standard over longer periods of time

**Table 1**Surface sediment  $^{87}\text{Sr}/^{86}\text{Sr}$ ,  $^{143}\text{Nd}/^{144}\text{Nd}$  and  $\epsilon_{\text{Nd}}$  from Fe–Mn coatings, detrital material and benthic foraminifers.  $2\sigma_{(\text{sd})}$  represents the external reproducibilities of repeated standard measurements.

Station	Latitude	Longitude	Depth [m]	$^{87}\text{Sr}/^{86}\text{Sr}_{\text{coating}}$	$2\sigma_{(\text{sd})}$	$^{143}\text{Nd}/^{144}\text{Nd}_{\text{coating}}$	$\epsilon_{\text{Nd}_{\text{coating}}}$	$2\sigma_{(\text{sd})}$	$^{87}\text{Sr}/^{86}\text{Sr}_{\text{detritus}}$	$2\sigma_{(\text{sd})}$	$^{143}\text{Nd}/^{144}\text{Nd}_{\text{detritus}}$	$\epsilon_{\text{Nd}_{\text{detritus}}}$	$2\sigma_{(\text{sd})}$	$^{143}\text{Nd}/^{144}\text{Nd}_{\text{foram}}$	$\epsilon_{\text{Nd}_{\text{foram}}}$	$2\sigma_{(\text{sd})}$
M772/067-2	01°45.14' S	82°37.47' W	2075	0.709077	3.20E-05	0.512679	0.8	1.0	0.708736	1.50E-05	0.512527	-2.2	0.1	–	–	–
M772/064-1	01°53.50' S	81°11.76' W	529	–	–	–	–	–	–	–	–	–	–	0.512753	2.2	0.4
M772/065-2	01°57.01' S	81°07.23' W	206	0.708816	3.20E-05	–	–	–	0.706146	1.50E-05	0.512637	0.0	0.1	0.512688	1.0	0.7
M772/072-2	02°49.01' S	81°00.53' W	425	–	–	–	–	–	–	–	–	–	–	0.512716	1.5	0.4
M772/069-2	03°16.02' S	80°56.87' W	339	0.708916	1.40E-05	0.512731	1.8	0.3	0.705084	1.50E-05	0.512582	-1.1	0.1	0.512720	1.6	0.7
M772/056-1	03°45.01' S	81°07.29' W	350	0.708847	3.20E-05	0.512638	0.0	0.3	0.708117	1.50E-05	0.512429	-4.1	0.1	0.512613	-0.5	0.7
M772/053-1	05°28.94' S	81°34.03' W	2607	0.708990	3.20E-05	0.512582	-1.1	0.3	0.710374	1.50E-05	0.512320	-6.2	0.1	–	–	–
M772/052-4	05°29.01' S	81°27.01' W	1255	–	–	–	–	–	–	–	–	–	–	0.512578	-1.2	0.7
M772/054-2	05°29.01' S	81°18.35' W	297	0.708788	3.20E-05	0.512598	-0.8	0.3	0.710489	1.50E-05	0.512333	-5.9	0.1	–	–	–
M772/047-3	07°52.01' S	80°31.36' W	625	0.709102	3.20E-05	0.512578	-1.2	0.3	0.707975	1.50E-05	0.512396	-4.7	0.1	0.512567	-1.4	0.7
M772/031-2	09°02.97' S	79°26.88' W	114	0.709111	3.20E-05	0.512578	-1.2	0.3	0.705873	1.50E-05	0.512508	-2.5	0.1	0.512558	-1.6	0.7
M772/028-1	09°17.69' S	79°53.86' W	1105	0.709037	3.20E-05	0.512579	-1.1	0.3	0.707777	1.50E-05	0.512384	-5.0	0.1	–	–	–
M772/029-4	09°17.70' S	79°37.11' W	433	–	–	–	–	–	–	–	–	–	–	0.512585	-1.0	0.4
M771/554	10°26.38' S	78°54.74' W	522	–	–	–	–	–	–	–	–	–	–	0.512563	-1.5	0.4
M772/026-2	10°45.13' S	78°28.43' W	425	–	–	–	–	–	–	–	–	–	–	0.512542	-1.9	0.4
M772/022-2	10°53.22' S	78°46.38' W	1923	0.708998	3.20E-05	0.512563	-1.5	0.3	0.707169	1.50E-05	0.512442	-3.8	0.1	–	–	–
M771/487	11°00.00' S	78°23.17' W	579	–	–	–	–	–	–	–	–	–	–	0.512595	-0.8	0.4
M771/519	11°00.01' S	78°16.28' W	410	–	–	–	–	–	–	–	–	–	–	0.512698	1.2	0.4
M771/520	11°00.02' S	78°01.87' W	196	0.709030	3.20E-05	0.512566	-1.4	0.5	0.708589	1.50E-05	0.512357	-5.5	0.1	–	–	–
M771/457	11°00.05' S	78°19.26' W	467	–	–	–	–	–	–	–	–	–	–	0.512628	-0.2	0.4
M771/458	11°00.12' S	78°25.59' W	698	0.709092	3.20E-05	0.512555	-1.6	1.0	0.707634	1.50E-05	0.512458	-3.5	0.1	0.512522	-2.3	0.7
M771/590	11°15.10' S	78°16.42' W	547	–	–	–	–	–	–	–	–	–	–	0.512616	-0.4	0.4
M771/602	11°16.04' S	78°18.38' W	618	0.709124	3.20E-05	0.512554	-1.6	1.0	0.707777	1.50E-05	0.512470	-3.3	0.1	0.512512	-2.5	0.7
M771/620	12°18.62' S	77°19.20' W	150	0.709001	1.40E-05	0.512569	-1.3	0.3	0.707487	1.40E-05	0.512475	-3.2	0.3	–	–	–
M771/611	12°29.47' S	77°27.96' W	417	–	–	–	–	–	–	–	–	–	–	0.512587	-1.0	0.4
M771/608	12°32.55' S	77°30.47' W	584	–	–	–	–	–	–	–	–	–	–	0.512556	-1.6	0.4
M772/002-4	15°04.75' S	75°44.00' W	290	0.709100	1.40E-05	0.512570	-1.3	0.3	0.708073	1.40E-05	0.512473	-3.2	0.3	–	–	–
M771/420	15°11.36' S	75°34.89' W	516	0.709160	1.40E-05	0.512550	-1.7	0.3	0.707958	1.40E-05	0.512501	-2.7	0.3	0.512564	-1.4	0.4
M771/403	17°26.00' S	71°51.41' W	296	0.709129	3.20E-05	0.512425	-4.2	0.5	0.707827	1.50E-05	0.512328	-6.0	0.1	–	–	–
M771/398	17°28.05' S	71°52.44' W	496	0.708920	3.20E-05	0.512408	-4.5	0.3	0.707180	1.50E-05	0.512315	-6.3	0.1	–	–	–
M771/409	17°38.36' S	71°58.25' W	920	0.708844	3.20E-05	0.512416	-4.3	0.3	0.707408	1.50E-05	0.512324	-6.1	0.1	–	–	–

**Table 2**  
Nearshore water column dissolved  $\epsilon_{\text{Nd}}$  values.  $2\sigma_{(\text{sd})}$  represents the external reproducibilities of repeated standard measurements.

Station	Latitude	Longitude	Bottom depth (m)	Water depth (m)	$\epsilon_{\text{Nd}}$	$2\sigma_{(\text{sd})}$	Reference
152	0°00'	85°50' W	2907	3	0.6	0.1	Grasse et al. (2012)
117	3°35' S	82°00' W	4048	90	-1.8	0.1	Grasse et al. (2012)
				2	-1.5	0.2	
				150	-2.3	0.1	
				398	-2.8	0.1	
				1487	-3.2	0.8	
				2473	-3.9	0.2	
125	6°00' S	82°00' W	5173	100	-2.3	0.4	This study
				806	8°00' S	79°51' W	138
807	10°00' S	78°23' W	111	80	-1.0	0.4	This study
				3	-1.5	0.6	
810	10°00' S	78°48' W	151	106	-4.2	0.5	This study
				3	-5.7	0.3	
812	10°00' S	79°08' W	331	300	-2.8	0.3	This study
2	10°00' S	80°00' W	6296	2	-2.7	0.3	Grasse et al. (2012)
				101	-1.7	0.3	
				498	-2.1	0.1	
				991	-2.3	0.1	
78	14°00' S	77°03' W	3026	2	-2.6	0.4	Grasse et al. (2012)
				199	-2.3	0.4	
				498	-2.5	0.4	
				1999	-3.2	0.3	
				2498	-4.7	0.3	
				2986	-3.6	0.3	
34	16°00' S	74°11' W	116	3	-3.9	0.3	This study
				111	-3.4	0.6	
30	16°00' S	75°33' W	6165	3	-3.4	0.4	Grasse et al. (2012)
				501	-2.9	0.5	
				1011	-3.4	0.4	
				3549	-4.3	0.5	
				4571	-4.9	0.5	
				5494	-4.5	0.5	

( $n = 20$  sessions within one year) gave an external reproducibility of 0.25‰ ( $2\sigma_{\text{sd}}$ ). All error bars provided in the figures either correspond to that external reproducibility or to the internal reproducibility if greater than 0.25‰.

### 2.3. Radiogenic neodymium and strontium isotope analyses

For dissolved Nd isotope analysis 20 L of seawater were collected using 12 L Niskin bottles and were directly transferred into previously acid cleaned LDPE cubitainers. The samples were filtered through 0.45  $\mu\text{m}$  nitrocellulose acetate filters (Millipore®) on board. All samples were acidified to pH 2 with concentrated subboiled hydrochloric acid (0.5 mL per litre). On board 500  $\mu\text{L}$  purified Fe(III)chloride solution ( $\sim 1$  g Fe(III)Cl/mL in 3 M HCl) were added to each 20 L sample and after one day of equilibration the samples were adjusted to pH 8 with ammonium hydroxide (25%, suprapur®) to co-precipitate the dissolved REEs with iron hydroxide. At GEOMAR REE separation from major element cations was performed using a cation exchange resin (0.8 mL BioRad® AG50W-X12 resin, mesh 200–400). The Nd was further purified in a second column chemistry step (2 mL Eichrom® Ln Spec, mesh 50–100). The applied column chemistry followed the methods of Barrat et al. (1996) and Le Fèvre and Pin (2005).

For Nd and Sr isotope analyses of the sediments, in a first step the carbonate fraction was removed from the freeze-dried and homogenised sediment samples using a 15%-acetic acid/1 M Na-acetate buffer solution. Thereafter, the authigenic Fe–Mn oxyhydroxide fraction containing the seawater-derived Nd and Sr was extracted from the sediment by leaching with a 0.05 M hydroxylamine hydrochloride/15%-acetic acid solution buffered to pH 3.8 with NaOH (Gutjahr et al., 2007; Stumpf et al., 2010). After

complete removal of the authigenic fraction 30 mg of the residual bulk fraction of the dried sediment was treated with a mixture of concentrated HF–HNO<sub>3</sub>–HCl until total dissolution for the extraction of the detrital radiogenic isotope signal was achieved. The elemental separation and purification of the leachates and of the completely dissolved detrital material followed previously published procedures for Sr (Horwitz et al., 1992) and Nd (Cohen et al., 1988) applying ion exchange chromatography for cation separation (0.8 mL AG50W-X12 resin, BioRad®, mesh 200–400) and subsequent separation of Sr from Rb (50  $\mu\text{L}$  Sr-Spec resin, mesh 50–100), as well as separation of Nd from the other REEs (2 mL Eichrom® Ln-Spec resin, mesh 50–100). The benthic foraminifers (bulk species) were picked from all size fractions  $>63$   $\mu\text{m}$ , because foraminiferal carbonate is scarce in this area of high diatom productivity. About 20 mg of benthic foraminiferal carbonate resulted in 5–10 ng of purified Nd for mass spectrometric analyses. The cleaning method of the foraminiferal carbonate applying oxidative and reductive cleaning procedures was carried out following the methods described by Boyle (1981), Vance and Burton (1999) and Vance et al. (2004). Due to the small amount of Nd in the foraminiferal carbonate and the simple matrix the chemical purification of Nd was achieved on a single column (3.14 mL Eichrom® Ln-Spec resin, mesh 50–100) (S. Kraft, pers. communication).

All radiogenic isotope measurements were performed on a NuPlasma HR MC-ICPMS (Nu Instruments) at GEOMAR. Measured Nd isotope compositions were corrected for instrumental mass bias using a <sup>146</sup>Nd/<sup>144</sup>Nd of 0.7219 and were normalised to the JNdi-1 standard with an accepted literature value for <sup>143</sup>Nd/<sup>144</sup>Nd of 0.512115 (Tanaka et al., 2000). External reproducibility was estimated by repeated measurements of the JNdi-1 standard and was between 15 and 55 ppm ( $2\sigma_{(\text{sd})}$ , Tables 1–3). Measured <sup>87</sup>Sr/<sup>86</sup>Sr

**Table 3**Downcore records of core SO147-106KL for  $\delta^{30}\text{Si}$  (bSiO<sub>2</sub> and picked diatoms),  $^{87}\text{Sr}/^{86}\text{Sr}$ ,  $^{143}\text{Nd}/^{144}\text{Nd}$  and  $\epsilon_{\text{Nd}}$  (Fe–Mn coatings and detrital material).

Age (cal. yr BP)	$\delta^{30}\text{Si}_{\text{bSiO}_2}$	$2\sigma_{(\text{sd})}$	$\delta^{30}\text{Si}_{\text{diatom}}$	$2\sigma_{(\text{sd})}$	$^{87}\text{Sr}/^{86}\text{Sr}_{\text{coating}}$	$2\sigma_{(\text{sd})}$	$^{143}\text{Nd}/^{144}\text{Nd}_{\text{coating}}$	$\epsilon_{\text{Nd}_{\text{coating}}}$	$2\sigma_{(\text{sd})}$	$^{87}\text{Sr}/^{86}\text{Sr}_{\text{detritus}}$	$2\sigma_{(\text{sd})}$	$^{143}\text{Nd}/^{144}\text{Nd}_{\text{detritus}}$	$\epsilon_{\text{Nd}_{\text{detritus}}}$	$2\sigma_{(\text{sd})}$
1169	–	–	1.38	0.11	0.709082	1.4E-05	0.512572	–1.3	0.3	0.708485	1.4E-05	0.512406	–4.5	0.3
1175	0.91	0.10	–	–	–	–	–	–	–	–	–	–	–	–
1334	1.11	0.21	–	–	–	–	–	–	–	–	–	–	–	–
1370	–	–	–	–	0.709128	1.4E-05	0.512585	–1.0	0.3	–	–	–	–	–
1388	0.94	0.18	–	–	–	–	–	–	–	–	–	–	–	–
1466	–	–	–	–	0.709117	1.4E-05	0.512583	–1.1	0.3	0.707750	1.4E-05	0.512451	–3.6	0.3
<sup>c</sup> Dupl.	–	–	–	–	0.709160	1.5E-05	0.512539	–1.9	0.3	–	–	–	–	–
1560	–	–	0.89	0.17	–	–	–	–	–	–	–	–	–	–
1578	1.10	0.10	–	–	–	–	–	–	–	–	–	–	–	–
1701	1.01	0.22	–	–	–	–	–	–	–	–	–	–	–	–
1725	–	–	–	–	0.709071	1.4E-05	0.512578	–1.2	0.3	–	–	–	–	–
1839	–	–	–	–	0.709125	1.4E-05	0.512604	–0.7	0.3	0.707292	1.4E-05	0.512487	–2.9	0.3
1860	1.26	0.24	–	–	–	–	–	–	–	–	–	–	–	–
2006	–	–	–	–	0.709132	1.4E-05	0.512576	–1.2	0.3	–	–	–	–	–
2449	0.80	0.13	–	–	–	–	–	–	–	–	–	–	–	–
3089	0.72	0.11	–	–	–	–	–	–	–	–	–	–	–	–
3130	–	–	0.83	0.10	0.709146	1.4E-05	0.512576	–1.2	0.3	0.706663	1.4E-05	0.512518	–2.3	0.3
3424	–	–	0.51	0.13	–	–	–	–	–	–	–	–	–	–
3470	0.83	0.18	–	–	–	–	–	–	–	–	–	–	–	–
3795	–	–	0.62	0.07	0.709149	1.4E-05	0.512541	–1.9	0.3	0.706719	1.4E-05	0.512521	–2.3	0.3
4182	–	–	–	–	0.709142	1.4E-05	0.512552	–1.7	0.3	–	–	–	–	–
<sup>c</sup> Dupl.	–	–	–	–	0.709150	1.5E-05	0.512558	–1.6	0.3	–	–	–	–	–
4407	–	–	–	–	0.709138	1.4E-05	0.512560	–1.5	0.3	0.706469	1.4E-05	0.512566	–1.4	0.3
4828	0.81	0.27	–	–	–	–	–	–	–	–	–	–	–	–
5943	–	–	0.42	0.22	–	–	–	–	–	–	–	–	–	–
8312	–	–	–	–	0.709168	1.4E-05	0.512564	–1.4	0.5	0.707013	1.4E-05	0.512548	–1.7	0.3
8370	0.39	0.24	–	–	–	–	–	–	–	–	–	–	–	–
8928	–	–	1.15	0.21	0.709158	1.4E-05	0.512590	–0.9	0.5	–	–	–	–	–
8950	–	–	–	–	0.709162	1.4E-05	0.512561	–1.5	0.5	0.707012	1.4E-05	0.512572	–1.3	0.3
9108	1.10	0.09	–	–	–	–	–	–	–	–	–	–	–	–
9170	–	–	–	–	0.709165	1.4E-05	0.512553	–1.7	0.5	0.706989	1.4E-05	0.512564	–1.5	0.3
9263	–	–	1.22	0.16	0.709155	1.4E-05	0.512561	–1.5	0.5	–	–	–	–	–
9276	1.01	0.28	–	–	–	–	–	–	–	–	–	–	–	–
9487	–	–	–	–	0.709168	1.4E-05	0.512560	–1.5	0.5	–	–	–	–	–
<sup>c</sup> Dupl.	–	–	–	–	–	–	0.512551	–1.7	0.5	–	–	–	–	–
9504	0.72	0.27	–	–	–	–	–	–	–	–	–	–	–	–
9523	–	–	–	–	0.709157	2.6E-05	0.512580	–1.1	0.5	0.707162	1.4E-05	0.512527	–2.2	0.3
9731	0.67	0.14	–	–	–	–	–	–	–	–	–	–	–	–
9796	–	–	–	–	0.709159	2.6E-05	0.512546	–1.8	0.5	0.707324	1.4E-05	0.512514	–2.4	0.3
9896	0.46	0.30	–	–	–	–	–	–	–	–	–	–	–	–
10,183	–	–	–	–	0.709181	2.6E-05	0.512586	–1.0	0.5	–	–	–	–	–
10,206	–	–	1.30	0.08	0.709163	2.6E-05	0.512571	–1.3	0.5	0.706966	1.4E-05	0.512509	–2.5	0.3
10,323	0.38	0.14	–	–	–	–	–	–	–	–	–	–	–	–
10,799	0.84	0.10	–	–	–	–	–	–	–	–	–	–	–	–
10,805	–	–	–	–	0.709141	2.6E-05	0.512565	–1.4	0.5	0.707154	1.4E-05	0.512532	–2.1	0.3
11,274	0.33	0.13	–	–	–	–	–	–	–	–	–	–	–	–
11,613	–	–	–	–	0.709148	2.6E-05	0.512568	–1.4	0.3	0.706571	1.5E-05	0.512545	–1.8	0.3
11,822	0.44	0.14	–	–	–	–	–	–	–	–	–	–	–	–
12,405	0.88	0.15	–	–	–	–	–	–	–	–	–	–	–	–
12,474	–	–	–	–	0.709117	2.6E-05	0.512542	–1.9	0.3	0.706476	1.5E-05	0.512556	–1.6	0.3
13,257	0.41	0.18	–	–	–	–	–	–	–	–	–	–	–	–
13,789	–	–	0.83	0.09	0.709136	2.6E-05	0.512560	–1.5	0.5	0.706507	1.5E-05	0.512571	–1.3	0.3
14,009	0.53	0.12	–	–	–	–	–	–	–	–	–	–	–	–
14,153	–	–	0.58	0.16	0.709119	2.6E-05	0.512569	–1.3	0.3	0.706203	1.5E-05	0.512597	–0.8	0.3

(continued on next page)

Table 3 (continued)

Age (cal. yr BP)	$\delta^{30}\text{Si}_{\text{diatom}}$	$\epsilon^{207}\text{Pb}/\text{Pb}_{\text{diatom}}$	$\delta^{30}\text{Si}_{\text{diatom}}$	$^{207}\text{Pb}/\text{Pb}_{\text{diatom}}$	$^{87}\text{Sr}/^{86}\text{Sr}_{\text{coating}}$	$b^{2\sigma}(\text{sd})$	$^{143}\text{Nd}/^{144}\text{Nd}_{\text{coating}}$	$\epsilon_{\text{Nd,coating}}$	$b^{2\sigma}(\text{sd})$	$^{87}\text{Sr}/^{86}\text{Sr}_{\text{detritus}}$	$b^{2\sigma}(\text{sd})$	$^{143}\text{Nd}/^{144}\text{Nd}_{\text{detritus}}$	$\epsilon_{\text{Nd,detritus}}$	$b^{2\sigma}(\text{sd})$
14,441	0.51	0.10	—	—	—	—	—	—	—	—	—	—	—	—
14,932	0.79	0.10	—	—	—	—	—	—	—	—	—	—	—	—
15,410	—	—	—	—	0.709096	2.6E-05	0.512546	-1.8	1.5E-05	0.706442	1.5E-05	0.512547	-1.8	0.3
<sup>a</sup> Dupl.	—	—	—	—	0.709105	1.5E-05	0.512529	-2.1	0.3	—	—	—	—	—
15,506	0.63	0.21	—	—	—	—	—	—	—	—	—	—	—	—
16,030	0.98	0.19	—	—	—	—	—	—	—	—	—	—	—	—
16,274	—	—	—	—	0.709117	2.6E-05	0.512572	-1.3	0.3	0.706408	1.5E-05	0.512567	-1.4	0.3
18,802	0.35	0.14	—	—	—	—	—	—	—	—	—	—	—	—
19,630	—	—	—	—	0.709123	2.6E-05	0.512550	-1.7	0.5	0.706283	1.5E-05	0.512604	-0.7	0.3

<sup>a</sup> External reproducibilities of repeated sample measurements.

<sup>b</sup> External reproducibilities of repeated standard measurements.

<sup>c</sup> Dupl. indicate duplicate samples.

ratios were corrected for instrumental mass bias using  $^{88}\text{Sr}/^{86}\text{Sr} = 8.3752$  and were normalised to the accepted value for NIST SRM987 of 0.710245. The  $2\sigma_{(\text{sd})}$  external reproducibility of repeated standard measurements was always better than 36 ppm ( $2\sigma_{(\text{sd})}$ , Tables 1 and 3). Total procedural blanks for leachates and total dissolution of the detrital material were  $\leq 83$  pg for Nd and 2.1 ng for Sr, respectively, which were negligible compared to sample concentrations.

### 3. Results

#### 3.1. $\epsilon_{\text{Nd}}$ Signatures extracted from waters and surface sediments

The Nd isotope composition of near-coastal waters and surface sediments from water depths between 114 m and 2607 m along the Ecuadorian and Peruvian shelf between the equator and 18°S was determined. The  $\epsilon_{\text{Nd}}$  signatures in the near-coastal water column range between -5.7 and +0.6 (Table 2). In the sediments (Table 1) the  $\epsilon_{\text{Nd,coating}}$  signatures supposedly representing seawater composition range from -4.5 to +1.8, whereas the Sr isotope compositions determined in the same fractions are between 0.70879 and 0.70916. Benthic foraminifera show  $\epsilon_{\text{Nd,foram}}$  values between -2.5 and +2.2. In the detrital material, the  $\epsilon_{\text{Nd,detritus}}$  ranges from -6.3 to 0 and from 0.70508 to 0.71049 for  $^{87}\text{Sr}/^{86}\text{Sr}_{\text{detritus}}$ .

All measured Nd isotope compositions of surface waters and sediments show an overall latitudinal trend from more radiogenic values in the north towards less radiogenic values in the south (Fig. 2b–e), which resembles the distribution of the Nd isotope compositions of the Andean hinterland rocks. From 0 to 4°S the dissolved, authigenic and detrital  $\epsilon_{\text{Nd}}$  signatures show an overall slight decrease (Fig. 2c). Along the central shelf from 4 to 14°S the authigenic signatures remain rather constant whereas the  $\epsilon_{\text{Nd}}$  of the detritus and the seawater show pronounced minimum values as low as -5 to -6 between 5°S and 11°S, which are not directly reflected in the Andean hinterland rocks. From 14 to 18°S the dissolved, authigenic and detrital  $\epsilon_{\text{Nd}}$  signatures are again shifted to less radiogenic values. South of 15°S no benthic foraminiferal  $\epsilon_{\text{Nd}}$  could be measured because the amount of available specimens in the sediments was too low.

The surface and subsurface waters show the largest variability, whereas the Nd isotope variability in the water column below is small (mean seawater  $\epsilon_{\text{Nd}} = -3.0 \pm 0.4$  (2 standard errors of the mean ( $2\sigma_{\text{sem}}$ ), (Fig. 3a). A trend towards less radiogenic isotope compositions with water depth is observed reaching values near -5 at depths below 4000 m (Fig. 3a).

In contrast to the overlying waters, the  $\epsilon_{\text{Nd}}$  signatures extracted from the surface sediments at different water depths show a large range (Fig. 3b). The authigenic  $\epsilon_{\text{Nd}}$  in the Fe–Mn coatings and benthic foraminifera from the subsurface waters (50 m–200 m water depth) are all very close to each other with a mean value of  $-1.4 \pm 0.2$  ( $2\sigma_{\text{sem}}$ , Fig. 3c). This is, within error, in good agreement with dissolved seawater measurements of the subsurface EUC further offshore near the equator (St. 152,  $\epsilon_{\text{Nd}} = -1.8 \pm 0.1$ , Grasse et al., 2012) and also with the mean value ( $\epsilon_{\text{Nd}} = -1.9 \pm 0.4$ ,  $2\sigma_{\text{sem}}$ ) obtained for subsurface water samples between 50 m and 200 m water depth along the Peruvian shelf in this study (Fig. 3c). Only the data at stations 807 and 34, which are located close to the coast, show less radiogenic  $\epsilon_{\text{Nd}}$  values between -3 and -4 for subsurface waters (Fig. 3c). In the intermediate waters between 200 m and 1000 m water depth, the  $\epsilon_{\text{Nd}}$  signature in the water column is less radiogenic than at the subsurface (mean  $\epsilon_{\text{Nd}} = -2.6 \pm 0.3$ ,  $2\sigma_{\text{sem}}$ ) (Fig. 3d). The authigenic fraction represented by the coatings and benthic foraminifera is overall significantly more radiogenic than the overlying waters (mean  $\epsilon_{\text{Nd}} = -1.3 \pm 0.6$ ,  $2\sigma_{\text{sem}}$ ) whereas the detrital fraction is less

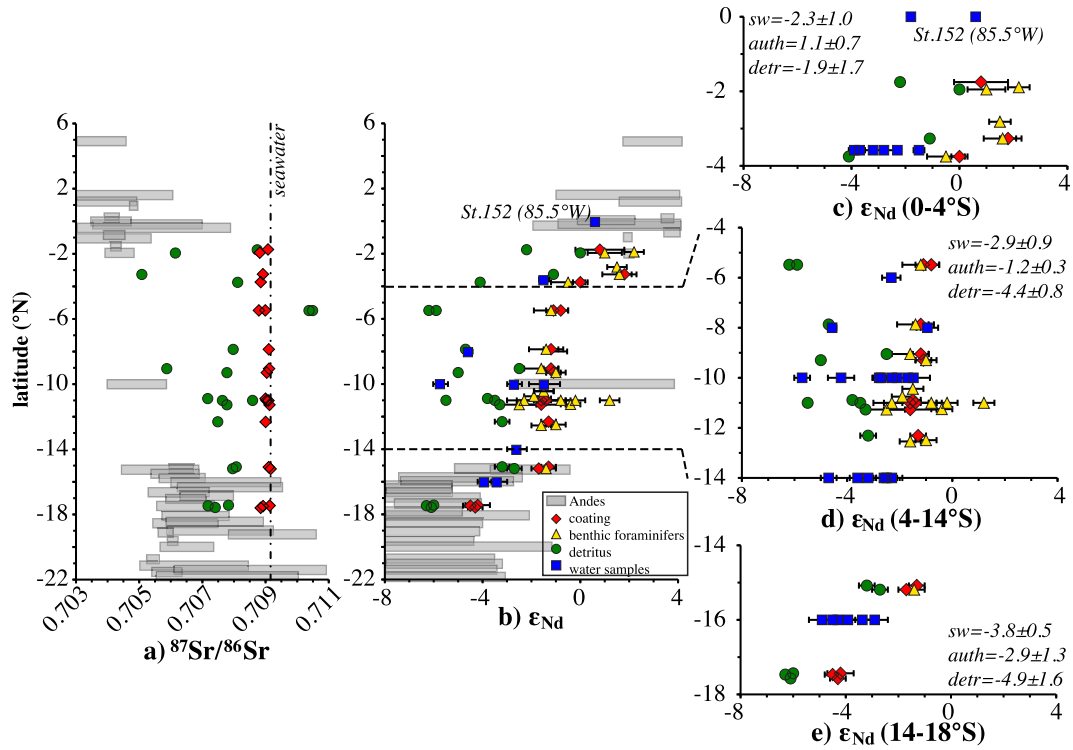


**Fig. 2.** Latitudinal distribution of a)  $^{87}\text{Sr}/^{86}\text{Sr}$ , the black dashed line indicates the present day dissolved seawater  $^{87}\text{Sr}/^{86}\text{Sr}$  of 0.70916, and b)  $\epsilon_{\text{Nd}}$  in surface waters and surface sediments along the Peruvian shelf: surface water dissolved  $\epsilon_{\text{Nd}}$  (blue squares), Fe–Mn coatings (red diamonds), benthic foraminifers (yellow triangles), and detrital material (green circles). The horizontal grey shadings mark the range of bulk rocks in the Andean hinterland (Sarbas and Nohl, 2009). c–e) Water column and sedimentary phases  $\epsilon_{\text{Nd}}$  for different latitudinal sections. The error bars represent  $2\sigma_{\text{(sd)}}$  external reproducibilities of repeated standard measurements. Given are the mean and  $2\sigma_{\text{sem}}$  range for the values of the seawater (sw), coating and benthic foraminifers (auth) and for the detritus (detr) for the respective latitudinal sections. (For interpretation of the references to colour in this figure legend, the reader is referred to the web version of this article.)

radiogenic (mean  $\epsilon_{\text{Nd}} = -4.3 \pm 1.8$ ,  $2\sigma_{\text{sem}}$ ) than the water. In deep waters below 1000 m the  $\epsilon_{\text{Nd}}$  signature of seawater and detrital fraction have similar values around  $-4$ , whereas the authigenic fraction remains more radiogenic at values around  $-0.8$  (Fig. 3e).

Overall the latitudinal variations of the detrital signal and the dissolved  $\epsilon_{\text{Nd}}$  in the surface waters generally covary (Fig. 2b). Within the subsurface waters, seawater and authigenic  $\epsilon_{\text{Nd}}$  are overall similar to each other with rather homogenous  $\epsilon_{\text{Nd}}$  values

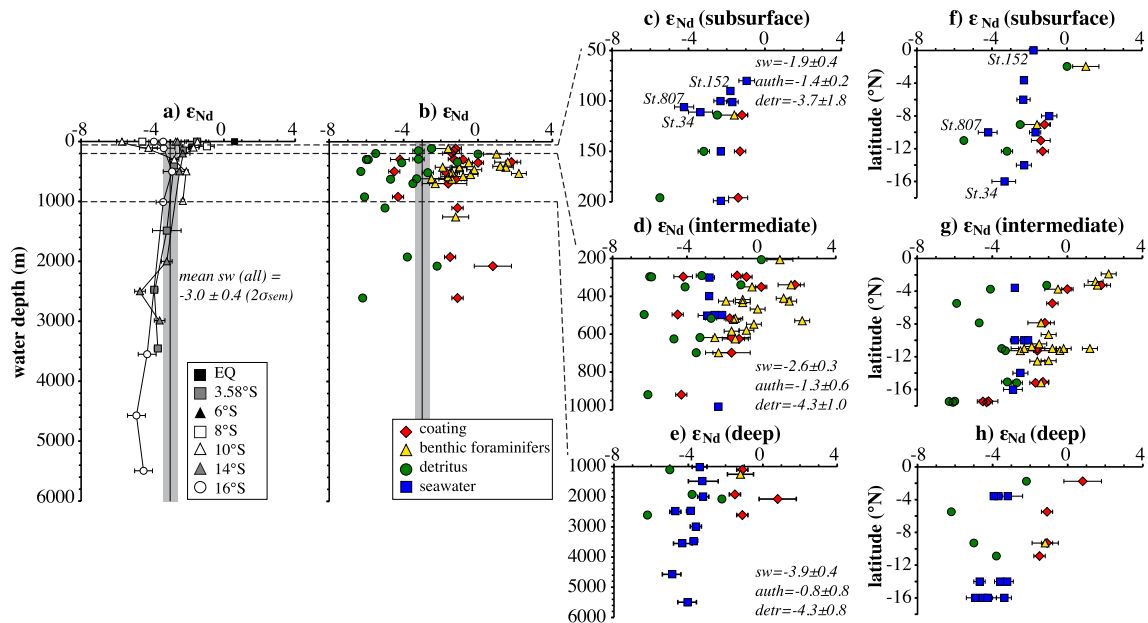


**Fig. 3.**  $\epsilon_{\text{Nd}}$  versus water depth for a) dissolved Nd isotopic composition, b) surface sediment Fe–Mn coatings (red diamonds), benthic foraminifers (yellow triangles) and detrital material (green circles). The error bars represent  $2\sigma_{\text{(sd)}}$  external reproducibilities of repeated standard measurements. c–e) represent the distribution within the subsurface layer (50–200 m water depth), intermediate waters (200–1000 m) and deep waters (>1000 m); f–h) represents the latitudinal distribution for all phases. Seawater samples in c–h) are indicated by blue squares. Given are the mean and  $2\sigma_{\text{sem}}$  range for the values of the seawater (sw), coating and benthic foraminifers (auth) and for the detritus (detr) in the respective water depths. (For interpretation of the references to colour in this figure legend, the reader is referred to the web version of this article.)

between  $-1.4$  and  $-1.9$  all along the shelf between the equator and  $16^\circ\text{S}$  (Fig. 3f). In the intermediate waters, the dissolved  $\epsilon_{\text{Nd}}$  again shows no clear trend, whereas the authigenic (both coatings and benthic foraminifera) overall decrease from North to South whereas the detrital sediment fraction shows pronouncedly unradiogenic values at  $4-8^\circ\text{S}$  and near  $16^\circ\text{S}$  (Fig. 3g).

The  $\epsilon_{\text{Nd}}$  signature of the Fe–Mn coatings and the benthic foraminifera is almost always at least 2 to 3  $\epsilon_{\text{Nd}}$  units more radiogenic than the respective detrital signal of the same samples or the dissolved Nd isotope composition. This offset is larger in the northern part of the study area and also becomes larger with increasing water depth (Fig. 3f–h). The  $\epsilon_{\text{Nd}}$  signatures of the Fe–Mn coatings and benthic foraminifera are mostly within error indistinguishable from each other (Fig. 4).

### 3.2. Downcore records

#### 3.2.1. Biogenic opal and silicon isotope compositions

In core SO147-106KL the bSiO<sub>2</sub> concentration shows a large variability between 3 wt% and 31 wt% (Fig. 5) (Wolf, 2002). Due to the fact that no dry bulk density (DBD) data were available for this core, we assumed a constant DBD of  $0.7 \text{ g/cm}^3 \cdot \text{ka}$  for the whole record to calculate a bSiO<sub>2</sub> mass accumulation rate (MAR) (Moore, 2008). The bSiO<sub>2</sub> MAR shows peak values for the early Holocene between 12 and 8 ka and during the late Holocene between 2.5 ka and present. Marked minimum bSiO<sub>2</sub> contents and MARs occurred during the LGM/deglacial before 12 ka and during the middle and late Holocene between 8 and 2.5 ka.

The  $\delta^{30}\text{Si}_{\text{opal}}$  signatures range from  $0.3\text{‰}$  to  $1.3\text{‰}$  for bSiO<sub>2</sub>, and from  $0.4\text{‰}$  to  $1.4\text{‰}$  for hand-picked diatoms (Fig. 5, Table 3). The results of both methods show the same overall trend and are mostly within error of each other with only one exception around 10.5 ka, where  $\delta^{30}\text{Si}_{\text{bSiO}_2}$  was low ( $+0.4\text{‰}$ ) and  $\delta^{30}\text{Si}_{\text{diatom}}$  was high ( $+1.3\text{‰}$ ). However, these values have not been produced from exactly the same samples, which means that this difference may still represent a reliable signal and may originate from the high annual or seasonal variability during that time. The lowest  $\delta^{30}\text{Si}_{\text{opal}}$  signatures occurred during the LGM ( $+0.3\text{‰}$ ) and during the deglacial (around  $+0.4\text{‰}$ ), whereas the early and late Holocene were characterised by higher values up to  $+1.4\text{‰}$ . Maxima and minima in bSiO<sub>2</sub> content and MAR, as well as in  $\delta^{30}\text{Si}_{\text{opal}}$  occurred around the same time.

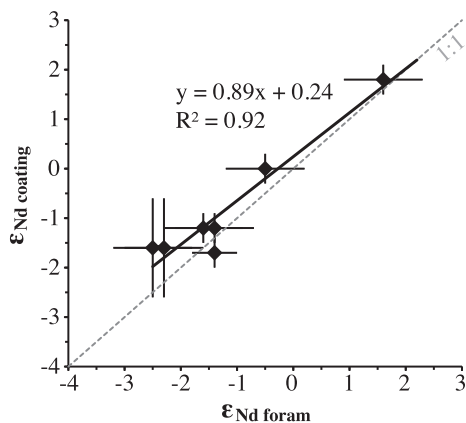


**Fig. 4.** Nd isotope composition of the benthic foraminifera versus the Fe–Mn coatings from the same samples. The grey dotted line represents a theoretical 1:1 correlation. Error bars represent  $2\sigma_{(\text{sd})}$  external reproducibilities of repeated standard measurements.

#### 3.2.2. Reliability of the silicon isotope data for environmental reconstructions

Recent results from culturing experiments suggesting a species-dependent fractionation factor (Sutton et al., 2013) raise the question whether a change in diatom assemblages may have been the cause for the observed downcore  $\delta^{30}\text{Si}_{\text{opal}}$  variations. For a core location similar to ours De Vries and Schrader (1981) found dominating tropical (low nutrient) diatom assemblages containing *Coscinodiscus* sp. for the period of time between 0 and 2.5 ka, thus indicating weaker upwelling conditions. At the same time, we find high  $\delta^{30}\text{Si}_{\text{opal}}$  values for both size fractions (Fig. 5), which is consistent with higher Si limitation. De Vries and Schrader (1981) also found particularly high *Chaetoceros* sp. abundances at  $\sim 16.1$  ka, a period of time characterised by relatively high  $\delta^{30}\text{Si}_{\text{opal}}$  values in our record (Fig. 5). Additionally, preliminary data from a sediment core further south at  $15^\circ\text{S}$  (unpublished diatom abundance data of X. Crosta and  $\delta^{30}\text{Si}_{\text{opal}}$  data of K. Doering, pers. communication) indicate that the lowest  $\delta^{30}\text{Si}_{\text{opal}}$  values, which in that core were also found in the LGM and deglacial sections, prevailed when upwelling indicating assemblages (containing *Chaetoceros* sp.) abundances were lowest, whereas high  $\delta^{30}\text{Si}_{\text{opal}}$  signatures were also associated with times of high *Chaetoceros* sp. abundances. Consequently, if a higher fractionation factor of  $-2.1\text{‰}$  for *Chaetoceros* sp. (Sutton et al., 2013) had significantly influenced the downcore record then high *Chaetoceros* sp. abundances would be associated with lower  $\delta^{30}\text{Si}_{\text{opal}}$  values, which is clearly not the case. Therefore, the downcore  $\delta^{30}\text{Si}$  signal in our record has most likely predominantly been controlled by changes in  $\text{Si}(\text{OH})_4$  utilisation and does not reflect changes of the diatom assemblage.

Downcore changes of the bSiO<sub>2</sub> and diatom assemblage records, however, do not necessarily only reflect changes in productivity, but may also have been influenced by changes in preservation (De Vries and Schrader, 1981). Settling diatoms are (partially) dissolved in the water column and in the sediment due to a combination of different physical, chemical and biological parameter (temperature, pressure, species composition, percentages of detrital silica, grazing, bacterial degradation of the protecting organic matrix around the diatom frustules) (Bidle and Azam, 1999; Ragueneau et al., 2000; Loucaides et al., 2012). However, the ratio of dissolution to production (D:P) in the water column along the Peruvian margin is relatively low ( $\sim 0.1$ ) (Nelson et al., 1981; Brzezinski et al., 2003), whereas the dissolution rate from the sediments is high. Dissolution of bSiO<sub>2</sub> is expected to lead to lower dissolved  $\delta^{30}\text{Si}_{\text{Si}(\text{OH})_4}$  values in the water column, which is potentially enhanced by the fractionation of Si isotopes during dissolution (Demarest et al., 2009) leaving the diatoms enriched in heavy  $^{30}\text{Si}$ . Such excursions (low bSiO<sub>2</sub> – high  $\delta^{30}\text{Si}_{\text{opal}}$ ) are, however, not observed in the record, which essentially rules out bSiO<sub>2</sub> dissolution as the main reason for the observed variability.

#### 3.2.3. Neodymium and strontium isotope signatures

For the downcore record unfortunately no  $\epsilon_{\text{Nd}_{\text{foram}}}$  could be determined due to the overall too low abundance of benthic foraminifera in the core. The downcore  $\epsilon_{\text{Nd}_{\text{coating}}}$  ( $^{87}\text{Sr}/^{86}\text{Sr}_{\text{coating}}$ ) signatures extracted from the Fe–Mn coatings range between  $-2.1$  (0.70907) and  $-0.9$  (0.70918) (Fig. 5, Table 3). The overall variability is low with no significant trends or excursions during the past 20 ka. In contrast, the  $\epsilon_{\text{Nd}_{\text{detritus}}}$  signatures range between  $-4.5$  and  $-0.7$  and show a trend from more radiogenic values during the LGM and the deglaciation to less radiogenic values during the late Holocene. The least radiogenic signatures occurred around 10 ka ( $\epsilon_{\text{Nd}_{\text{detritus}}} \sim -2.5$ ) and in particular during the past 2.5 ka ( $\epsilon_{\text{Nd}_{\text{detritus}}} \sim -4.5$ ), which represents the most pronounced change recorded. The  $^{87}\text{Sr}/^{86}\text{Sr}_{\text{detritus}}$  signature of the detrital fraction

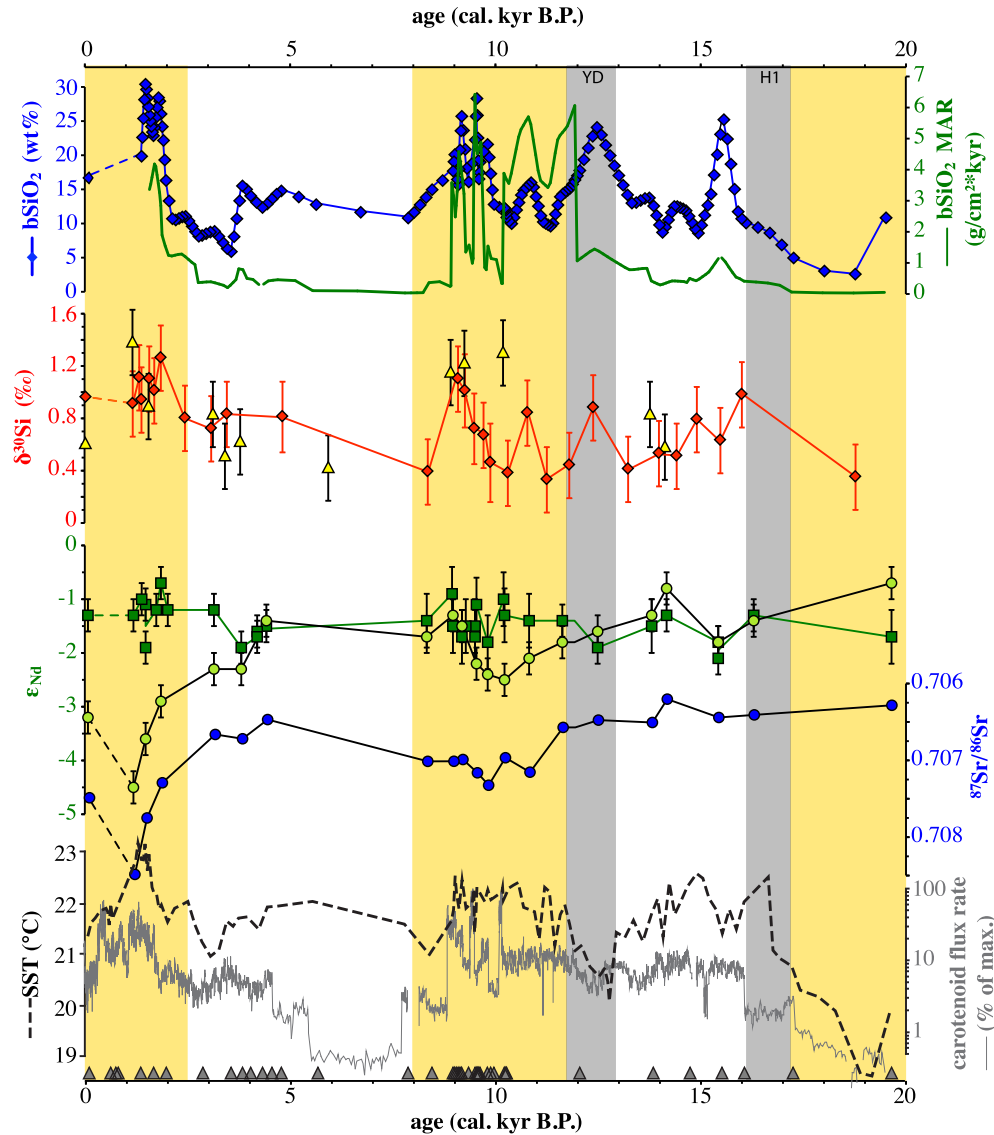


**Fig. 5.** Downcore records of core SO147-106KL for bSiO<sub>2</sub> concentration (wt%) (Wolf, 2002); bSiO<sub>2</sub> MAR (g/cm<sup>2</sup>ka); δ<sup>30</sup>Si (‰) of bSiO<sub>2</sub> (red diamonds) and hand-picked diatoms (yellow triangles), the youngest samples represent mean values from the area of the strongest upwelling between 5 and 15°S (see Ehlert et al., 2012), and error bars represent 2σ<sub>(sd)</sub> external reproducibilities of repeated sample measurements; ε<sub>Nd</sub><sup>detr</sup> (light green circles) and ε<sub>Nd</sub><sup>coating</sup> (dark green squares), whereby the youngest samples represent surface sediment data closest to the core location (see surface samples, this study), error bars represent 2σ<sub>(sd)</sub> external reproducibilities of repeated standard measurements; and <sup>87</sup>Sr/<sup>86</sup>Sr<sub>detr</sub> (light blue circles, scale is reversed); alkenone derived sea surface temperatures SST (°C) and carotenoid flux rate (% of maximum) (Rein et al., 2005). The grey triangles represent calibrated AMS <sup>14</sup>C dates of the organic carbon fraction (Rein et al., 2004, 2005). Vertical yellow shadings mark the time slices specifically discussed in the text. (For interpretation of the references to colour in this figure legend, the reader is referred to the web version of this article.)

ranged between 0.70620 and 0.70849 and shows a variability closely following that of the ε<sub>Nd</sub><sup>detr</sup> record (Fig. 5, Table 3).

## 4. Discussion

### 4.1. Neodymium and strontium isotope composition in waters and surface sediments

Along the Peruvian shelf the ε<sub>Nd</sub> signature of the authigenic Fe–Mn coatings, the benthic foraminifers, both of which are generally taken to represent the isotopic composition of past bottom waters, and the detrital fraction all show a general overall trend from more radiogenic values in the north to less radiogenic values in the south. The values decrease from the Equator to 4°S, are more variable with no clear trend along the central shelf from 4 to 14°S and decrease again south of 14°S (Fig. 2). This is similar to the general

distribution of the dissolved seawater ε<sub>Nd</sub> signature (Grasse et al., 2012; and this study). The waters, authigenic fractions and the detrital particles exhibit Nd (and Sr) isotope signatures similar to those of the hinterland rocks in the Andes (Fig. 2b), which are characterised by highly radiogenic (unradiogenic) values between +4 and +7 (around 0.705 and lower) near the equator and less (more) radiogenic values of up to –6 (0.706 and higher) in central and southern Peru and northern Chile (source regions are defined here as: equator (0–5°N), northern Peru and Ecuador (0–5°S), central Peru (5–15°S), southern Peru (15–18°S), and northern Chile (18–22°S)) (Sarbas and Nohl, 2009).

#### 4.1.1. Dissolved ε<sub>Nd</sub> in nearshore Peruvian waters

The Nd isotope compositions of the surface waters in the study area are highly variable (Figs. 2b and 3a), whereas all subsurface, intermediate and deep water masses near the shelf are less variable

and show only a slight trend towards less radiogenic values with depth (Fig. 3c–e) and with latitude towards the south (Fig. 3f–h). In general, the water mass Nd isotope signatures and mixtures in the EEP are dominated by three main endmembers: the Southern Ocean characterised by less radiogenic signatures between  $-5$  and  $-9$  (Piepgras and Wasserburg, 1982; Stichel et al., 2012) and the northern and central Pacific with more radiogenic  $\epsilon_{\text{Nd}}$  signatures between  $-5$  and  $-2$  (Piepgras and Jacobsen, 1988; Amakawa et al., 2009). Along the continental margin the water column profiles show comparably radiogenic  $\epsilon_{\text{Nd}}$  values around  $-1.9$  within the subsurface layer representing the EUC/PCUC (Fig. 3c, f) (Lacan and Jeandel, 2001; Grasse et al., 2012). Below until 2000 m water depth only a slight trend towards less radiogenic values is observed, which, however, does not allow a clear identification of distinct signatures for different water masses.

#### 4.1.2. Authigenic $\epsilon_{\text{Nd}}$ as a recorder of past seawater Nd isotope composition

All sedimentary phases display a relatively large scatter of  $\epsilon_{\text{Nd}}$  signatures with water depth and latitude. The overall  $\epsilon_{\text{Nd}}$  patterns of seawater and authigenic phases are similar. However, the authigenic phases offset to more radiogenic values by 2–3  $\epsilon_{\text{Nd}}$  units compared to the actual seawater signatures (Fig. 3). The apparent offset is larger in the northern part of the study area and seems to increase with water depth (Fig. 3f–h). There are several possible reasons for this observation, all of which have to remain speculative in this study.

Water column Nd isotope compositions from further offshore (e.g. St. 152, and other stations from Grasse et al., 2012) indicate delivery of highly radiogenic dissolved  $\epsilon_{\text{Nd}}$  signatures from the Panama Basin. This suggests that the more radiogenic than expected authigenic  $\epsilon_{\text{Nd}}$  signatures in all water depths along the northern shelf may indeed originate from seawater. The misfit between seawater and authigenic  $\epsilon_{\text{Nd}}$  signatures may thus be a sampling artifact (missing water column data near the shelf in the northern part of the study area) or may indicate that the measured seawater values were only a snapshot of unusual conditions with increased influence of water masses with less radiogenic  $\epsilon_{\text{Nd}}$  signatures during the sampling period. In contrast, the authigenic phases may represent the integrated mean of a longer time period, probably several years to decades, when the southward transport of more radiogenic water masses was stronger. In the subsurface water (50 m–200 m water depth), the signatures of the Fe–Mn coatings and the benthic foraminifers, which overall agree in their isotope signatures (Fig. 4), reflect the dissolved  $\epsilon_{\text{Nd}}$  signature of the subsurface waters (Fig. 3c, f). With respect to the above discussion it is noteworthy that water column station 34, which is located at  $16^{\circ}\text{S}$ , has slightly less radiogenic signatures. ADCP profiles obtained during the sampling period in January 2009 at that latitude indicate a stronger than normal influence of the northward directed PCoastalC down to 250 m depth, which is usually confined to very shallow depths near the surface (Czeschel et al., 2011). This may have influenced the instantaneous signature in the water column, but is not reflected in the sediments, which integrate the signal over longer timescales.

The presented distribution of more radiogenic than expected authigenic Nd isotope values in the surface sediments is most likely an effect of the time integrated influence of the incoming central Pacific surface waters carrying highly positive  $\epsilon_{\text{Nd}}$  values (Lacan and Jeandel, 2001; Grasse et al., 2012) and exchange with the detrital fraction of the shelf sediments together with minor effects of downslope transport of particles. In addition, the measured water column  $\epsilon_{\text{Nd}}$  values, which fail to explain the highly radiogenic authigenic signatures in the sediment, probably do not reflect the predominant current patterns along the shelf area over longer time periods. In summary, the available data suggest that the  $\epsilon_{\text{Nd}}^{\text{auth}}$  signature extracted from Peruvian shelf sediment cannot be used as

a quantitative water mass tracer for the paleo reconstructions but may at best only serve as a qualitative indicator of changes.

#### 4.1.3. Exchange with detrital sediments

The actual dissolved seawater  $\epsilon_{\text{Nd}}$  values show a trend towards less radiogenic signatures towards the South (Fig. 2c–e). Although this trend is weak it is similar to the trend in the detrital material. This might indicate gradual exchange processes between seawater and detritus and thus may not represent water mass mixing.

Boundary exchange with the underlying sediments, continuous eolian or riverine material input from the Andean hinterland and partial dissolution of this material and subsequent mixing with the advected dissolved isotopic signatures (Tachikawa et al., 2004; Lacan and Jeandel, 2005; Grasse et al., 2012) can influence the local water mass signatures. Especially the anoxic sediments of the Peruvian shelf have to be considered as a source for Nd (Elderfield and Sholkovitz, 1987; Haley et al., 2004). Input of detrital material along the Peruvian shelf is dominated by riverine input, whereas the deposition of dust delivered from the arid Peruvian Andes and, to a lesser extent, from the Atacama Desert (Molina-Cruz, 1977; Saukel et al., 2011), is less important (Scheidegger and Krissek, 1982; Bruland et al., 2005). The surface water dissolved  $\epsilon_{\text{Nd}}$  signatures display a wide range and mirror the hinterland geology and the isotopic compositions of the exposed rocks (Fig. 2b). Two pronounced minimum values can be found at  $8^{\circ}\text{S}$  and  $10^{\circ}\text{S}$ , which are however still in the range of the detrital signatures. The  $\epsilon_{\text{Nd}}$  signatures of the authigenic phases follow the signatures of the rocks in the hinterland. For intermediate water depths down to 1000 m the authigenic sedimentary phases show a north-south trend, whereas the water column remains at signatures only slightly less radiogenic than the subsurface layer (Fig. 3g, f).

In deeper water depths the authigenic signatures remain more radiogenic than the overlying waters. Recent studies have shown, that the leaching of sediments can preferentially mobilise minor reactive components such as volcanic material with a much more radiogenic signature than the bulk detrital sediment (e.g., Tachikawa et al., 2004; Vance et al., 2004; Wilson et al., 2013). This should not be the case for the extraction of the Nd isotope composition from foraminifers. However, both authigenic phases agree well to each other (Figs. 2 and 4).

Off Peru, downslope transport of particles can occur during earthquakes (Dorbath et al., 1990; Reinhardt et al., 2002) or more continuously within a nepheloid layer along the steep continental margin, which has been invoked before to explain uniform authigenic Nd isotope signatures extracted from continental slope sediments (Gutjahr et al., 2008; Stumpf et al., 2010). This process can significantly influence the Nd isotope distribution in Fe–Mn coatings, but should leave the benthic foraminifera unaffected, which is why sediment redistribution cannot be the dominating process.

In contrast to the authigenic signatures, provenance analysis shows that the trend in detrital  $\epsilon_{\text{Nd}}$  and Sr isotope signatures of all surface sediment samples can be explained by southwards increasing contributions of central and southern Peruvian origin (Figs. 2 and 6), which have significantly less radiogenic  $\epsilon_{\text{Nd}}$  and more radiogenic  $^{87}\text{Sr}/^{86}\text{Sr}$  isotope signatures than the source rocks in the northern part of the study area near the equator. Thus past changes in provenance of the detrital material is interpreted in terms of changes in transport of particles by variations in the speed and origin of the currents.

#### 4.2. Environmental conditions on the central Peruvian shelf during the past 20 ka

The Peruvian coastal upwelling region has been very sensitive to the ENSO system, which strongly affects circulation, upwelling

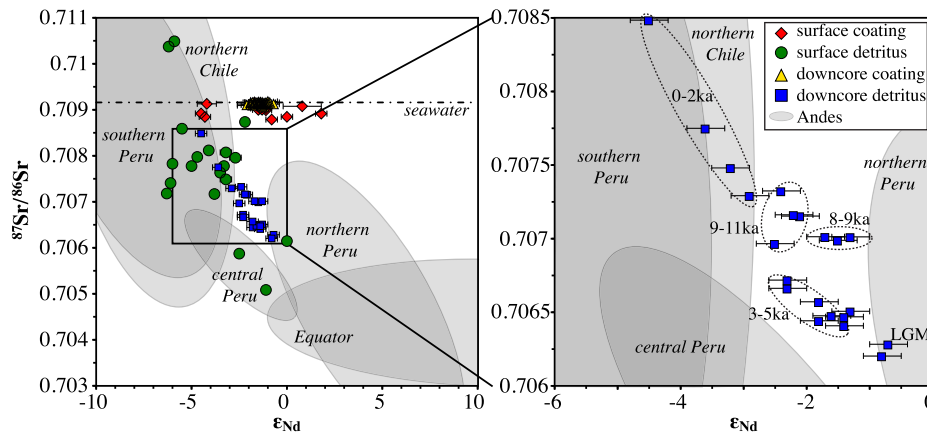


**Fig. 6.**  $\epsilon_{Nd}$  versus  $^{87}Sr/^{86}Sr$  for surface sediment and downcore data together with potential source endmembers indicating the provenance of the detrital material (same data source as for Fig. 3; Sarbas and Nohl, 2009). Error bars represent  $2\sigma_{(sd)}$  external reproducibilities of repeated standard measurements. The dashed circles mark time periods of significant changes in the radiogenic isotope composition discussed in the text.

intensity (Brink et al., 1983), primary biological productivity (Fiedler, 2002; Pennington et al., 2006) and the rainfall regime (Bendix, 2000; Baker et al., 2001). Paleo records suggest persistent ENSO variability at millennial timescales throughout the Last Glacial–interglacial cycle, but overall weaker El Niño intensity (lower frequency and amplitude of major events) seems to have prevailed during the latest Pleistocene and the first half of the Holocene, with respect to the late Holocene (Rodbell et al., 1999; Tudhope et al., 2001). However, this interpretation is not consistent in all records. For example, carotenoid pigment data by Rein et al. (2005) reveal high primary productivity during the early and late Holocene (Fig. 5), which has been related to enhanced upwelling and nutrient supply due to higher La Niña intensity. In contrast, alkenone-derived SSTs (Rein et al., 2005) indicate that highest temperatures/weakest upwelling and therefore weakest nutrient re-supply from subsurface waters also occurred during these periods of time (Fig. 5). These contradictory results may be a consequence of the sedimentary integration of different archives recording the opposing ENSO states. The combined proxy records of  $\epsilon_{Nd}$ ,  $bSiO_2$  MAR and  $\delta^{30}Si_{opal}$  in our study now provide a unique window into past ENSO variability and document fundamental changes in upwelling and nutrient supply conditions during the past 20 ka. El Niño- and La Niña-like conditions alternating on seasonal and interannual timescales left their signal in the sedimentary record.

#### 4.2.1. Past changes in circulation and upwelling intensity

The  $\epsilon_{Nd_{coating}}$  record does not indicate any major changes water mass provenance over the past 20 ka. Clearly at the shallow site of core 106KL (184 m water depth, 12°S) a significant change in circulation and water mass mixing would be expected for changes in upwelling intensity in that under strong upwelling conditions the strongest influence of the southward flowing subsurface waters (e.g. PCUC) should have occurred. Under weaker upwelling conditions, associated with a widening of the thermocline, the influence of northward directed surface currents, such as the PCC or the PCoastalC may have been increased (Huyer et al., 1987). However, Grasse et al. (2012) have shown that the surface waters along the coast display a wide range in  $\epsilon_{Nd}$  while the subsurface waters below do not differ significantly in their  $\epsilon_{Nd}$  signature, which is supported by the new data presented in this study (Fig. 3a). Thus, a change in  $\epsilon_{Nd_{coating}}$  may not be observable even if changes in mixing relationships between these water masses occurred.

In contrast, the  $\epsilon_{Nd_{detritus}}$  signature has varied significantly during the investigated period of time, ranging from more radiogenic  $\epsilon_{Nd}$  values around  $-1$  during the LGM and deglacial to less radiogenic

values around  $-2.5$  during the early Holocene and in particular during the late Holocene to values around  $-4.5$ . More radiogenic  $\epsilon_{Nd_{detritus}}$  values are related to a more northerly source region in the Peruvian and Ecuadorian hinterland (Figs. 2b and 6), whereas less radiogenic values are ascribed to a more local origin from central or southern Peruvian sources. During times of strong upwelling, which are associated with predominant La Niña-like conditions, the southward movement of water masses was strong, and consequently material with a distinctly more radiogenic  $\epsilon_{Nd}$  signatures can be transported from north to south along the shelf to the core location. Vice versa, during times of dominant El Niño-like conditions when upwelling diminished, the southward flowing currents were weaker and delivered less material to the core location. These time periods have mostly been associated with higher rainfall in the hinterland resulting in higher supply of material from the nearby local hinterland (Bendix, 2000; Baker et al., 2001).

#### 4.2.2. Past silicic acid utilisation by diatoms in the surface waters

**4.2.2.1. Downcore relationship between  $\delta^{30}Si_{opal}$  and  $bSiO_2$  MAR and quantitative reconstruction of silicic acid utilisation.** The record of core SO147-106KL does not only reveal a markedly lower  $bSiO_2$  content in the glacial and deglacial sediments prior to 13 ka, but also a large variability during the past 20 ka (Fig. 5). The content of  $bSiO_2$  was high ( $>20$  wt%) during the late Holocene (1–2.5 ka), the early Holocene (9–10 ka), the Younger Dryas (YD) and immediately after Heinrich event 1 (15–16 ka). When considering  $bSiO_2$  MARs, the evolution looks somewhat different and reveals enhanced but highly variable diatom accumulation only during the early (9–12 ka) and late Holocene (after  $\sim 2.5$  ka). The  $\delta^{30}Si_{opal}$  records for both diatom size fractions (11–32  $\mu m$  and 125–250  $\mu m$ ) show a variability very similar to the  $bSiO_2$  content with lower values around  $+0.4\text{‰}$  indicating low  $Si(OH)_4$  utilisation during the deglacial and highest values around  $+1.4\text{‰}$  indicating strong  $Si(OH)_4$  utilisation during the early and late Holocene (Fig. 5).

The theoretical relationship between the degree of surface water  $Si(OH)_4$  utilisation and the Si isotope composition can be described assuming either Rayleigh-type (fixed input followed by fractional loss or export) or steady state (constant supply and export at equilibrium) fractionation behaviour (Fig. 7). The lighter isotopes are preferentially incorporated into the diatom frustules leaving the dissolved fraction enriched in the heavier isotopes (Douthitt, 1982; De La Rocha et al., 1997). Assuming that all recorded  $\delta^{30}Si_{opal}$  variations are only a function of  $Si(OH)_4$  utilisation in the surface waters, this would imply that the highest  $\delta^{30}Si_{opal}$  occurred when there was near complete utilisation of  $Si(OH)_4$

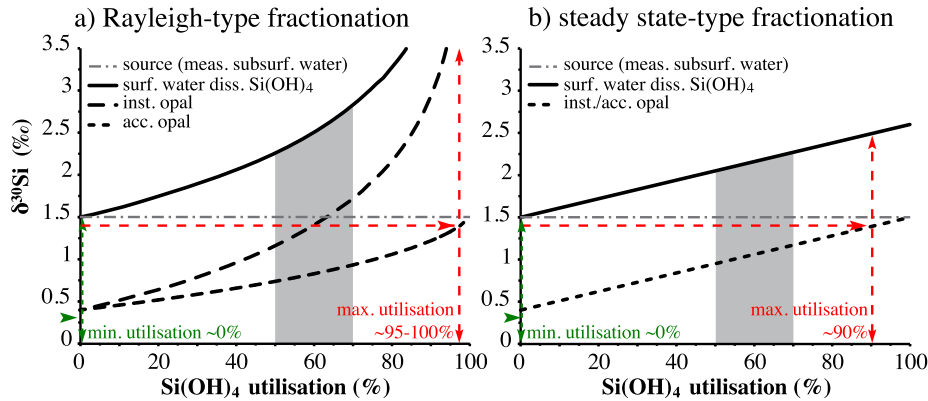


**Fig. 7.** Theoretical changes in  $\delta^{30}\text{Si}$  values of seawater (solid lines) and instantaneous and accumulated bSiO<sub>2</sub> (dashed and pointed lines) as a function of Si(OH)<sub>4</sub> utilisation from the available pool with an initial  $\delta^{30}\text{Si}$  value of +1.5‰. Precipitation of opal follows either a) a Rayleigh-type fractionation model or b) a steady state system behaviour applying a fractionation factor of  $-1.1\text{‰}$  (De La Rocha et al., 1997). The grey shading represents the observed present day surface water utilisation in the area between 5°S and 15°S (the main upwelling region) ranging between 50 and 70% (Ehlert et al., 2012). Horizontal arrows mark maximum (late Holocene, red dashed arrow)  $\delta^{30}\text{Si}_{\text{opal}}$  values of +1.4‰ and respective Si(OH)<sub>4</sub> utilisation of 95–100% (a) and 90% (b). Minimum utilisation (LGM and deglacial, green dotted arrow) for the lowest  $\delta^{30}\text{Si}_{\text{opal}}$  around 0.3‰ is around 0%. (For interpretation of the references to colour in this figure legend, the reader is referred to the web version of this article.)

(Reynolds et al., 2008; Pichevin et al., 2012). At complete utilisation the  $\delta^{30}\text{Si}_{\text{opal}}$  would be equal to the dissolved  $\delta^{30}\text{Si}_{\text{Si(OH)}_4}$  of the source water (= +1.4‰) (Fig. 7). This value is in good agreement with actual measurements of  $\delta^{30}\text{Si}_{\text{Si(OH)}_4}$  from the present-day upwelling subsurface source waters ( $\delta^{30}\text{Si}_{\text{Si(OH)}_4} = +1.5\text{‰}$ , Ehlert et al., 2012) indicating that the highest  $\delta^{30}\text{Si}_{\text{opal}}$  values during the early and late Holocene reflect near-complete Si(OH)<sub>4</sub> utilisation.

Present day surface waters in the area of the core location (between 5°S and 15°S) have relatively low  $\delta^{30}\text{Si}_{\text{Si(OH)}_4}$  between +1.7‰ and 2‰, because the re-supply of Si(OH)<sub>4</sub> via upwelling is relatively constant, and the fractionation due to limitation is low. The degree of Si(OH)<sub>4</sub> utilisation is only between 50 and 70% (Fig. 7). The  $\delta^{30}\text{Si}_{\text{opal}}$  record of the past 20 ka shows a large variability, whereby the highest values (+1.4‰) measured in samples from the late Holocene are in good agreement with values found today in the regions of weak upwelling. They indicate surface water  $\delta^{30}\text{Si}_{\text{Si(OH)}_4}$  values of +2.5‰ assuming a fractionation factor between diatoms and seawater of  $-1.1\text{‰}$  (De La Rocha et al., 1997). The respective calculated surface water utilisation of Si(OH)<sub>4</sub> ranges between 90% and 100% depending on which fractionation model is applied (for Rayleigh-type fractionation Fig. 7a and for steady state-type fractionation Fig. 7b). The lowest  $\delta^{30}\text{Si}_{\text{opal}}$  values (+0.3 to +0.4‰) in the downcore record, which occurred during the deglacial and which were accompanied by minima in bSiO<sub>2</sub> MARs, consequently indicate lower surface water dissolved  $\delta^{30}\text{Si}_{\text{Si(OH)}_4}$  values of about +1.4‰. These low values correspond to those of the present day subsurface source water and are only insignificantly lower than what is found today in the areas of strongest upwelling along the Peruvian shelf (Ehlert et al., 2012). This corresponds to an almost absent utilisation of Si(OH)<sub>4</sub> in the surface water for both types of fractionation if the source waters supplying the surface waters remained at the same Si isotope signatures as observed today (Fig. 7).

Today the  $\delta^{30}\text{Si}$  source signature is mainly delivered via the EUC, which has a  $\delta^{30}\text{Si}_{\text{Si(OH)}_4}$  signature of +1.5‰ (Beucher et al., 2008; Ehlert et al., 2012). During the Last Glacial, however, this source signature may have been different due to changes in the preformed Si(OH)<sub>4</sub> concentration and origin of the source water (Brzezinski et al., 2002; De La Rocha and Bickle, 2005; Reynolds et al., 2008), a changed utilisation or remineralisation processes along the EUC flowpath, or a reorganisation of the circulation in the region (Crosta et al., 2007; Leduc et al., 2010). Therefore, much lower  $\delta^{30}\text{Si}_{\text{opal}}$  values are reasonable and are consistent with an overall reduced productivity and Si(OH)<sub>4</sub> utilisation. Assuming the same source

signature for the source waters would indicate very low Si(OH)<sub>4</sub> utilisation, because  $\delta^{30}\text{Si}_{\text{opal}}$  was only about +0.3‰, and consequently the surface water  $\delta^{30}\text{Si}_{\text{Si(OH)}_4}$  above was only +1.4‰, indicating almost absent Si(OH)<sub>4</sub> utilisation (Fig. 7) (Ehlert et al., 2012).

However, there are several possibilities to interpret the  $\delta^{30}\text{Si}_{\text{opal}}$  data, which will be discussed in the following.

**4.2.2.2. Silicic acid versus iron limitation.** In the EEP the availability of Si(OH)<sub>4</sub> in surface waters is considered to be the major controlling factor of bSiO<sub>2</sub> productivity (Dugdale and Wilkerson, 1998; Pennington et al., 2006; Warnock et al., 2007), which is consistent with recent findings of surface sediment calibration studies indicating low utilisation rates in areas of high nutrient availability and high productivity (Egan et al., 2012; Ehlert et al., 2012). In the downcore record, however, high opal content and MARs correspond to high  $\delta^{30}\text{Si}_{\text{opal}}$  indicating high Si(OH)<sub>4</sub> utilisation. This is contrary to the observed present day distribution because low bSiO<sub>2</sub> accumulation would have been expected to occur as a consequence of a limitation of Si(OH)<sub>4</sub> supply, which would then have caused a higher fractionation of the silicon isotopes and thus higher  $\delta^{30}\text{Si}$  (De La Rocha et al., 1998). Brodie and Kemp (1994), however, suggested that upwelling events trigger diatom blooms and high opal accumulation in the sediments. This suggests that the combined records of high bSiO<sub>2</sub> MAR and high  $\delta^{30}\text{Si}_{\text{opal}}$ , e.g. during the early and late Holocene, indicate the prevalence of (periodically) occurring La Niña-like conditions.

An alternative explanation for the observed correlation between bSiO<sub>2</sub> MARs and  $\delta^{30}\text{Si}_{\text{opal}}$  could also be that diatom growth along the Peruvian upwelling area in the past was not ultimately limited by Si(OH)<sub>4</sub> supply, but that other micro- or macronutrients, such as Fe or P, controlled diatom productivity (see also Moore et al., 2004; Pichevin et al., 2009, 2012; Brzezinski et al., 2011). Diatoms have a high demand for these elements during growth (Sunda and Huntsman, 1995). In the EEP the major inputs of Fe and P originate from remineralisation processes in the anoxic shelf sediments (Froelich et al., 1988; Scholz et al., 2011). This source is most efficient under strongly oxygen-depleted bottom water conditions (Ingall and Jahnke, 1994; McManus et al., 1997). Several studies (e.g. Gutiérrez et al., 2009; Fuenzalida et al., 2009) have shown that the upper boundary of the OMZ in the water column has varied over time, mostly related to pronounced El Niño events, during which the upwelling-driven nutrient supply to the

euphotic zone along the Peruvian shelf was reduced (Huyer et al., 1987). This has led to decreased primary productivity (Feldman et al., 1984; Chavez, 2005), less oxygen consumption through decay of organic matter, which in turn has led to decreased Fe and P supply from the underlying sediments. Under Fe-limited conditions, however, diatoms reveal a higher Si:N uptake ratio (they are more strongly silicified, but also more likely  $\text{Si}(\text{OH})_4$  limited) (Takeda, 1998; Hutchins et al., 2002; Baines et al., 2010) which leads to an increased export of Si (via  $\text{bSiO}_2$ ) relative to N and which affects the interpretation of the  $\text{bSiO}_2$  record in terms of nutrient utilisation. Consequently, the highest  $\text{bSiO}_2$  contents in the sediment, especially in the late and the early Holocene, could reflect such periods of time, during which upwelling was at least temporarily reduced (due to El-Niño like conditions) resulting in a reduced Fe-supply from the sediments enhancing  $\text{Si}(\text{OH})_4$  limitation because of the increased Si-demand under Fe-limiting conditions. Comparison with high (coccolithophorid) alkenone-derived sea surface temperatures (SSTs) supports this conclusion of reduced upwelling during those periods of time (Fig. 5) (Rein et al., 2005). However, coccolithophorids and diatoms represent different seasons of upwelling conditions. High carotenoid pigment fluxes at times of high opal accumulation rather indicate a true increase in productivity and not only a relative increase in silicification. In addition, the shallow, near-shore location of the core and thus most likely continuous supply make an influence of Fe-limitation on the preserved opal accumulation and  $\text{Si}(\text{OH})_4$  utilisation signal less likely.

In the following, the paleoenvironmental reconstruction for three distinct time slices, the (De)glacial, the early Holocene and the late Holocene, will be discussed in detail.

#### 4.2.3. Reconstruction of the LGM and deglacial conditions (prior to 13 ka)

Several studies have proposed that during the Last Glacial period unused  $\text{Si}(\text{OH})_4$  from the Southern Ocean was transported into the tropical upwelling areas via Subantarctic Mode Water, where it supposedly promoted enhanced diatom over coccolithophorid productivity (Silicic Acid Leakage Hypothesis – SALH) (e.g. Nozaki and Yamamoto, 2001; Brzezinski et al., 2002; Matsumoto and Sarmiento, 2008; Arellano-Torres et al., 2011). However, several recent studies observed the opposite to expected evolutions of opal production and deposition. Low glacial opal burial rates in the EEP (Pichevin et al., 2009; Dubois et al., 2010) may have occurred due to increased Fe input. Others argued that the low glacial  $\text{bSiO}_2$  productivity may have occurred due to persistent El Niño-like conditions in the tropical Pacific (Bradtmillier et al., 2006), which weakened upwelling and therefore decreased  $\text{Si}(\text{OH})_4$  and Fe supply to the euphotic zone. Alternatively, the missing increase in low latitude opal productivity may indicate a Pacific-wide overall reduced nutrient concentration and therefore nutrient supply to the tropics within thermocline waters during the Last Glacial due to reduced vertical mixing in the Southern Ocean (Loubere et al., 2011), which would have limited productivity independent of the strength of upwelling. Indeed, the carotenoid pigment data and the  $\text{bSiO}_2$  MAR indicate greatly reduced productivity prior to at least 16 ka, while  $\delta^{30}\text{Si}_{\text{opal}}$  and utilisation rates were low. In contrast to the present situation dust-related Fe input in the EEP was at least 30% higher during the glacial (McGee et al., 2007), which probably contributed to weaker silicification of the diatoms and thus also lower  $\text{Si}(\text{OH})_4$  utilisation. Nevertheless, our data do overall not support the arrival of enhanced glacial  $\text{Si}(\text{OH})_4$  supply from the Southern Ocean resulting in higher diatom productivity as predicted by the SALH.

After the LGM (between 18 and 15.5 ka), Higginson and Altabet (2004) found an increased coccolithophorid over diatom

productivity off Peru. A depleted pool of  $\text{Si}(\text{OH})_4$  from the Southern Ocean, which reached the Peruvian upwelling region via SAMW caused a reduction in the availability of Si relative to that of N, favouring coccolithophorid productivity and causing an increase in the  $\delta^{30}\text{Si}_{\text{opal}}$  to values around 1.0‰ at 15 ka (Fig. 5). From 15.5 to ~13 ka the system reversed. Diatom productivity increased over coccolithophorid productivity (Higginson and Altabet, 2004), and  $\delta^{30}\text{Si}_{\text{opal}}$  decreased again to low values (Fig. 5) indicating an increased availability of  $\text{Si}(\text{OH})_4$ .

The Last Glacial detrital radiogenic isotope signatures were most radiogenic in  $\epsilon_{\text{Nd}_{\text{detritus}}}$  and least radiogenic for  $^{87}\text{Sr}/^{86}\text{Sr}_{\text{detritus}}$ , indicating strong contributions from northern Peru (Fig. 5). A possible prevalence of El Niño-like conditions would have resulted in enhanced rainfall, which delivered larger amounts of local detrital material with less radiogenic  $\epsilon_{\text{Nd}_{\text{detritus}}}$  and more radiogenic  $^{87}\text{Sr}/^{86}\text{Sr}_{\text{detritus}}$  signatures to the shelf (Fig. 3a, b). Independent indications for such a process are, however, missing during the Last Glacial. Therefore, we propose that the Peruvian shelf was not influenced by El Niño-like conditions but rather characterised by stronger upwelling of low-nutrient waters delivering material from the North with at least periodical nutrient supply from subsurface waters and enhanced productivity.

#### 4.2.4. The early Holocene (12–8 ka)

In contrast to the LGM and Deglacial,  $\text{bSiO}_2$  MAR and content were high (~20 wt%) during the early Holocene at the location of the core (Fig. 5). At the same time, the  $\delta^{30}\text{Si}_{\text{opal}}$  increased to values around +1.2‰, which is higher than the values measured in modern surface sediments in that area ( $\delta^{30}\text{Si} \sim +0.6$  to  $+0.9$ ‰) (Ehlert et al., 2012). De Vries and Schrader (1981) argued that high diatom concentration along the Peruvian shelf during the late Pleistocene may have been related to a switch in diatom assemblage towards more dissolution-resistant species (due to a slight northward shift of the upwelling cell from 14–16°S to 12–14°S, in which the diatoms are more dissolution-resistant). However, our relatively high  $\delta^{30}\text{Si}_{\text{opal}}$  values and carotenoid pigment concentrations near 9.5 ka show that the change in  $\text{bSiO}_2$  content in the record was related to a real change in  $\text{Si}(\text{OH})_4$  utilisation and productivity and was not only a consequence of enhanced preservation. Simultaneously increased  $\text{bSiO}_2$  MARs and high  $\delta^{30}\text{Si}_{\text{opal}}$  values indicate higher nutrient concentrations in the water column but also higher  $\text{Si}(\text{OH})_4$  utilisation between 8 and 10 ka due to periodically intensified La Niña-like conditions. During that time, the SSTs were higher than during most of the remainder of the record (Fig. 5) (Rein et al., 2005) indicating at least seasonally weaker upwelling during El Niño-like conditions.

During the early Holocene, between 12 and 10 ka, the  $\epsilon_{\text{Nd}_{\text{detritus}}}$  showed a trend towards less radiogenic signatures reaching values as low as –2.5 (Fig. 5). At the same time the  $^{87}\text{Sr}/^{86}\text{Sr}_{\text{detritus}}$  increased moderately. During the subsequent early Holocene, however, the trend reversed and the  $\epsilon_{\text{Nd}_{\text{detritus}}}$  returned to values around –1.5, whereas the  $^{87}\text{Sr}/^{86}\text{Sr}_{\text{detritus}}$  remained unchanged. These trends indicate a change of the atmospheric circulation. Alternating El Niño- and La Niña-like conditions most likely prevailed causing periodically higher local material input with less radiogenic  $\epsilon_{\text{Nd}_{\text{detritus}}}$  signatures and more radiogenic  $^{87}\text{Sr}/^{86}\text{Sr}_{\text{detritus}}$  values due to enhanced rainfall. Although the SSTs were high, the trend in  $\epsilon_{\text{Nd}_{\text{detritus}}}$  from less radiogenic towards more radiogenic values from 10 to 9 ka most likely resulted from a shift from more El Niño-like towards more La Niña-like conditions with stronger upwelling accompanied by a subsurface current strengthening and a shift of the provenance from more southern towards more central Peruvian origin (Fig. 6). Under stronger upwelling conditions, the material transport within the southward directed currents (PCUC) was obviously enhanced.

Similar to our observations of bSiO<sub>2</sub> MAR and Si(OH)<sub>4</sub> utilisation, and in contrast to the results by Rein et al. (2005), Carré et al. (2005) found that SSTs in southern Peru were about 3 °C colder during the early Holocene compared to the late Holocene, indicating stronger upwelling conditions during that time. Vargas et al. (2006) on the other hand found several debris flows in southernmost Peru dated for the time period 12.9 to 8.4 ka BP, which were interpreted to be associated with intense rainfall episodes that must have occurred during non-El Niño conditions, concomitant with intensified coastal upwelling. These different findings indicate a high variability of the system alternating between El Niño and La Niña conditions during the early Holocene with warm SSTs, variable primary bioproductivity and strong El Niño related flooding events.

#### 4.2.5. The late Holocene off Peru (2.5–1 ka)

All applied proxies document a highly variable environment along the Peruvian shelf during the late Holocene. The bSiO<sub>2</sub> MAR, similar to the carotenoid pigment fluxes, increased strongly around 2 ka resulting in high sedimentary bSiO<sub>2</sub> contents up to 20–30 wt%. This was accompanied by the highest δ<sup>30</sup>Si<sub>opal</sub> signatures of up to +1.4‰. Calculating surface water δ<sup>30</sup>Si<sub>Si(OH)<sub>4</sub></sub> values of +2.5‰ results in estimates for Si(OH)<sub>4</sub> utilisation between 90 and 100% (Fig. 7), which represents the highest level during the past 20 ka. A 90% utilisation can today only be found in those areas of weaker upwelling and lower nutrient re-supply to the surface water (Ehlert et al., 2012). During the late Holocene the ε<sub>Nd,detr</sub> signal showed the largest variability within the past 20 ka. It was characterised by a pronounced decrease from –1.5 to values around –4.5 between 4 and 1.2 ka. The surface sediment in that area is also characterised by less radiogenic ε<sub>Nd,detr</sub> values around –3.2 compared to the areas further north. In particular, the signatures of the last 2 ka were very different from the rest of the record. The highly unradiogenic ε<sub>Nd,detr</sub> and radiogenic <sup>87</sup>Sr/<sup>86</sup>Sr<sub>detr</sub> would be consistent with enhanced dust input from the Atacama Desert in southern Peru and northern Chile (Fig. 6) (Molina-Cruz, 1977). However, climatic reconstructions indicate a general southward shift in the mean position of the Intertropical Convergence Zone during the Holocene (Haug et al., 2001), which caused higher precipitation in the Peruvian region (Bendix, 2000; Baker et al., 2001) and thus a more locally dominated input of material. At the same time high bSiO<sub>2</sub> content and high Si(OH)<sub>4</sub> utilisation required stronger upwelling of nutrient-rich subsurface waters, which usually occurs during La Niña-like conditions. The observed timing and high variability in our record confirms that, although the early Holocene record shows some characteristics of high ENSO intensity, very strong ENSO patterns only operated during the second half of the Holocene and that the onset of modern ENSO conditions did not occur prior to 5.5 ka BP, with increased frequency of major events only during recent times (Loubere et al., 2003; Carré et al., 2005; Vargas et al., 2006; Toth et al., 2012). It was only during the latest Holocene of the past 2–3 ka that the Peruvian shelf area experienced persistently more moderate productivity conditions, with shorter periods of increased productivity (Agnihotri et al., 2008).

## 5. Conclusions

Surface sediments along the Peruvian margin were analysed for their radiogenic Nd isotope composition, and compared to water column measurements from the same area. In general, all phases (seawater, Fe–Mn coatings, benthic foraminifers and detrital material) display a trend from more radiogenic values in the North towards less radiogenic values in the South, which is in good agreement with the distribution of the signatures of the outcropping rocks of the Andean hinterland. Authigenic ε<sub>Nd</sub> signatures are mostly significantly more radiogenic than the seawater or detrital

phases. This probably reflects the authigenic signatures being influenced by highly radiogenic water masses originating from the Panama basin that were not present along the shelf during the sampling period in 2009. However, neither the dissolved seawater ε<sub>Nd</sub> nor the authigenic phases show distinct signatures for certain water masses, which makes it difficult to use the ε<sub>Nd,auth</sub> signatures as water mass tracers. The ε<sub>Nd,detr</sub>, on the other hand, reflects local weathering inputs and hinterland geology and material transport via currents.

Combined bSiO<sub>2</sub> content and MAR, δ<sup>30</sup>Si<sub>opal</sub>, ε<sub>Nd</sub> and <sup>87</sup>Sr/<sup>86</sup>Sr in coatings and detrital material have been analysed to reconstruct surface water Si(OH)<sub>4</sub> utilisation by diatoms and upwelling intensity during the past 20 ka. During most of the past 20 ka both bSiO<sub>2</sub> content and δ<sup>30</sup>Si<sub>opal</sub> were low, which is attributed to the fact that diatom productivity along the Peruvian shelf was ultimately limited by Si(OH)<sub>4</sub> availability. Overall low Si(OH)<sub>4</sub> concentrations in Pacific thermocline waters did not allow large diatom blooming events. During times of high ENSO intensity periodically strong upwelling (e.g. the late Holocene but also partly during the early Holocene) caused high nutrient supply and intense diatom blooming associated with high Si(OH)<sub>4</sub> utilisation rates. The Nd and Sr isotope signatures of the detrital material support this interpretation. Both time periods were characterised by relatively unradiogenic ε<sub>Nd</sub> and radiogenic <sup>87</sup>Sr/<sup>86</sup>Sr signatures characteristic for material input directly from the hinterland. This input mainly occurred via riverine discharge during El Niño (-like) conditions, when rainfall was high and upwelling intensity was low. Accordingly, the early and the late Holocene were probably also the periods of the strongest variations of the Peruvian OMZ. The combined evidence from bSiO<sub>2</sub> MAR, δ<sup>30</sup>Si<sub>opal</sub> and the radiogenic Nd and Sr isotope compositions of the detrital material documents that the strongest ENSO conditions of the past 20 ka have only prevailed during the past 5 ka.

## Acknowledgements

This work is a contribution of the Sonderforschungsbereich 754 "Climate–Biogeochemistry Interactions in the Tropical Ocean" ([www.sfb754.de](http://www.sfb754.de)) which is supported by the Deutsche Forschungsgemeinschaft. We are thankful for the constructive suggestions of two anonymous reviewers and the editorial handling by C. Hillaire-Marcel.

## References

- Abrantes, F., Lopes, C., Mix, A.C., Pisias, N.G., 2007. Diatoms in southeast Pacific surface sediments reflect environmental properties. *Quaternary Science Reviews* 26 (1–2), 155–169. <http://dx.doi.org/10.1016/j.quascirev.2006.02.022>.
- Agnihotri, R., Altabet, M.A., Herbert, T.D., Tierney, J.E., 2008. Subdecadally resolved paleoceanography of the Peru margin during the last two millennia. *Geochemistry Geophysics Geosystems* 9, Q05013. <http://dx.doi.org/10.1029/2007GC001744>.
- Albarède, F., Telouk, P., Blichert-Toft, J., Boyet, M., Agranier, A., Nelson, B.K., 2004. Precise and accurate isotopic measurements using multiple-collector ICPMS. *Geochimica et Cosmochimica Acta* 68 (12), 2725–2744. <http://dx.doi.org/10.1016/j.gca.2003.11.024>.
- Amakawa, H., Sasaki, K., Ebihara, M., 2009. Nd isotopic composition in the central North Pacific. *Geochimica et Cosmochimica Acta* 73 (16), 4705–4719. <http://dx.doi.org/10.1016/j.gca.2009.05.058>.
- Arellano-Torres, E., Pichevin, L.E., Ganeshram, R.S., 2011. High-resolution opal records from the eastern tropical Pacific provide evidence for silicic acid leakage from HNLC regions during glacial periods. *Quaternary Science Reviews* 30 (9–10), 1112–1121. <http://dx.doi.org/10.1016/j.quascirev.2011.02.002>.
- Baines, S.B., Twining, B.S., Brzezinski, M.A., Nelson, D.M., Fisher, N.S., 2010. Causes and biogeochemical implications of regional differences in silicification of marine diatoms. *Global Biogeochemical Cycles* 24, GB4031. <http://dx.doi.org/10.1029/2010GB003856>.
- Baker, P.A., Seltzer, G.O., Fritz, S.C., Dunbar, R.B., Grove, M.J., Tapia, P.M., Cross, S.L., Rowe, H.D., Broda, J.P., 2001. The history of South American tropical precipitation for the past 25,000 years. *Science* 291, 640–643. <http://dx.doi.org/10.1126/science.291.5504.640>.

- Barber, R.T., Chavez, F.P., 1983. Biological consequences of El Niño. *Science* 222, 1203–1210. <http://dx.doi.org/10.1126/science.222.4629.1203>.
- Barrat, J.A., Keller, F., Amossé, J., Taylor, R.N., Nesbitt, R.W., Hirata, T., 1996. Determination of Rare Earth Elements in sixteen silicate reference samples by ICP-MS after Tm addition and ion exchange separation. *Geostandards Newsletter* 20 (1), 133–139.
- Bendix, J., 2000. Precipitation dynamics in Ecuador and northern Peru during the 1991/92 El Niño: a remote sensing perspective. *International Journal of Remote Sensing* 21 (3), 533–548.
- Beucher, C.P., Brzezinski, M.A., Jones, J.L., 2008. Sources and biological fractionation of Silicon isotopes in the Eastern Equatorial Pacific. *Geochimica et Cosmochimica Acta* 72 (13), 3063–3073. <http://dx.doi.org/10.1016/j.gca.2008.04.021>.
- Beucher, C.P., Brzezinski, M.A., Jones, J.L., 2011. Mechanisms controlling silicon isotope distribution in the Eastern Equatorial Pacific. *Geochimica et Cosmochimica Acta* 75, 4286–4294. <http://dx.doi.org/10.1016/j.gca.2011.05.024>.
- Bidle, K.D., Azam, F., 1999. Accelerated dissolution of diatom silica by marine bacterial assemblages. *Nature* 397, 508–512.
- Bostock, H.C., Opydyke, B.N., Williams, M.J.M., 2010. Characterising the intermediate depth waters of the Pacific Ocean using  $\delta^{13}\text{C}$  and other geochemical tracers. *Deep-Sea Research* 157 (7), 847–859. <http://dx.doi.org/10.1016/j.dsr.2010.04.005>.
- Boyle, E.A., 1981. Cadmium, zinc, copper and barium in foraminifera tests. *Earth and Planetary Science Letters* 53, 11–35.
- Bradt Miller, L.L., Anderson, R.F., Fleisher, M.Q., Burckle, L.H., 2006. Diatom productivity in the equatorial Pacific Ocean from the last glacial period to the present: a test of the silicic acid leakage hypothesis. *Paleoceanography* 21, PA4201. <http://dx.doi.org/10.1029/2006PA001282>.
- Brink, K.H., Halpern, D., Huyer, A., Smith, R.L., 1983. The physical environment of the Peruvian upwelling system. *Progress in Oceanography* 12, 285–305.
- Brodie, I., Kemp, A.E.S., 1994. Variation in biogenic and detrital fluxes and formation of laminae in late Quaternary sediments from the Peruvian coastal upwelling zone. *Marine Geology* 116 (3–4), 385–398. [http://dx.doi.org/10.1016/0025-3227\(94\)90053-1](http://dx.doi.org/10.1016/0025-3227(94)90053-1).
- Bruland, K.W., Rue, E.L., Smith, G.J., DiTullio, G.R., 2005. Iron, macronutrients and diatom blooms in the Peru upwelling regime: brown and blue waters of Peru. *Marine Chemistry* 93 (2–4), 81–103. <http://dx.doi.org/10.1016/j.marchem.2004.06.011>.
- Brzezinski, M.A., et al., 2011. Co-limitation of diatoms by iron and silicic acid in the equatorial Pacific. *Deep-Sea Research II* 58 (3–4), 493–511. <http://dx.doi.org/10.1016/j.dsr2.2010.08.005>.
- Brzezinski, M.A., Jones, J.L., Bidle, K.D., Azam, F., 2003. The balance between silica production and silica dissolution in the sea: insights from Monterey Bay, California, applied to the global data set. *Limnology and Oceanography* 48 (5), 1846–1854.
- Brzezinski, M.A., Pride, C.J., Franck, V.M., Sigman, D.M., Sarmiento, J.L., Matsumoto, K., Gruber, N., Rau, G.H., Coale, K.H., 2002. A switch from  $\text{Si}(\text{OH})_4$  to  $\text{NO}_3^-$  depletion in the glacial Southern Ocean. *Geophysical Research Letters* 29 (12), 3–6. <http://dx.doi.org/10.1029/2001GL014349>.
- Carré, M., Bentealeb, I., Fontugne, M., Lavallée, D., 2005. Strong El Niño events during the early Holocene: stable isotope evidence from Peruvian sea shells. *The Holocene* 15, 42–47. <http://dx.doi.org/10.1191/0959683605h1782rp>.
- Chavez, F.P., 2005. Biological consequences of interannual to multidecadal variability. In: Robinson, A., Brink, K.H. (Eds.), *The Sea*, vol. 13. Harvard University Press, Cambridge, pp. 643–679.
- Cohen, A.S., O’Nions, R.K., Siegenthaler, R., Griffin, W.L., 1988. Chronology of the pressure-temperature history recorded by a granulite terrain. *Contributions to Mineralogy and Petrology* 98, 303–311.
- Crosta, X., Beucher, C.P., Pahnke, K., Brzezinski, M.A., 2007. Silicic acid leakage from the Southern Ocean: opposing effects of nutrient uptake and oceanic circulation. *Geophysical Research Letters* 34, L13601. <http://dx.doi.org/10.1029/2006GL029083>.
- Czeschel, R., Stramma, L., Schwarzkopf, F.U., Giese, B.S., Funk, A., Karstensen, J., 2011. Middepth circulation of the eastern tropical South Pacific and its link to the oxygen minimum zone. *Journal of Geophysical Research* 116, C01015. <http://dx.doi.org/10.1029/2010JC006565>.
- De La Rocha, C.L., Bickle, M.J., 2005. Sensitivity of silicon isotopes to whole-ocean changes in the silica cycle. *Marine Geology* 217 (3–4), 267–282. <http://dx.doi.org/10.1016/j.margeo.2004.11.016>.
- De La Rocha, C.L., Brzezinski, M.A., DeNiro, M.J., 1997. Fractionation of silicon isotopes by marine diatoms during biogenic silica formation. *Geochimica et Cosmochimica Acta* 61 (23), 5051–5056. [http://dx.doi.org/10.1016/S0016-7037\(97\)00300-1](http://dx.doi.org/10.1016/S0016-7037(97)00300-1).
- De La Rocha, C.L., Brzezinski, M.A., DeNiro, M.J., 1998. Silicon-isotope composition of diatoms as an indicator of past oceanic change. *Nature* 395, 680–683.
- Demarest, M.S., Brzezinski, M.A., Beucher, C.P., 2009. Fractionation of silicon isotopes during biogenic silica dissolution. *Geochimica et Cosmochimica Acta* 73 (19), 5572–5583. <http://dx.doi.org/10.1016/j.gca.2009.06.019>.
- DeMaster, D.J., 1981. The supply and accumulation of silica in the marine environment. *Geochimica et Cosmochimica Acta* 45 (10), 1715–1732. [http://dx.doi.org/10.1016/0016-7037\(81\)90006-5](http://dx.doi.org/10.1016/0016-7037(81)90006-5).
- De Souza, G.F., Reynolds, B.C., Rickli, J., Frank, M., Saito, M.A., Gerringa, L.J.A., Bourdon, B., 2012. Southern Ocean control of silicon stable isotope distribution in the deep Atlantic Ocean. *Global Biogeochemical Cycles* 26, GB2035. <http://dx.doi.org/10.1029/2011GB004141>.
- De Vries, T.J., Schrader, H., 1981. Variations of upwelling/oceanic conditions during the latest Pleistocene through Holocene off the central Peruvian coast: a diatom record. *Marine Micropaleontology* 6, 157–167.
- Dia, A., Dupré, B., Allègre, C.J., 1992. Nd isotopes in Indian Ocean sediments used as a tracer of supply to the ocean and circulation paths. *Marine Geology* 103, 349–359.
- Dorbath, L., Cisternas, A., Dorbath, C., 1990. Assessment of the size of large and great historical earthquakes in Peru. *Bulletin of the Seismological Society of America* 80 (3), 551–576.
- Douthitt, C.B., 1982. The geochemistry of the stable isotopes of silicon. *Geochimica et Cosmochimica Acta* 46, 1449–1458.
- Dubois, N., Kienast, M., Kienast, S.S., Calvert, S.E., François, R., Anderson, R.F., 2010. Sedimentary opal records in the eastern equatorial Pacific: It is not all about leakage. *Global Biogeochemical Cycles* 24, GB4020. <http://dx.doi.org/10.1029/2010GB003821>.
- Dugdale, R.C., Wilkerson, F.P., 1998. Silicate regulation of new production in the equatorial Pacific upwelling. *Nature* 391, 270–273.
- Dugdale, R.C., Wischmeyer, A.G., Wilkerson, F.P., Barber, R.T., Chai, F., Jiang, M.-S., Peng, T.-H., 2002. Meridional asymmetry of source nutrients to the equatorial Pacific upwelling ecosystem and its potential impact on ocean–atmosphere  $\text{CO}_2$  flux: a data and modeling approach. *Deep-Sea Research II* 49, 2513–2531.
- Dullo, W.-C., Rein, B., Wolf, A., Biebow, N., Schrader, K., Sirocco, F., 2000. Core descriptions and reflectance spectra. In: *Sonne SO147 Cruise Report*, pp. 102–112.
- Egan, K.E., Rickaby, R.E.M., Leng, M.J., Hendry, K.R., Hermoso, M., Sloane, H.J., Bostock, H.C., Halliday, A.N., 2012. Diatom silicon isotopes as a proxy for silicic acid utilisation: a Southern Ocean core top calibration. *Geochimica et Cosmochimica Acta*. <http://dx.doi.org/10.1016/j.gca.2012.08.002>.
- Ehlert, C., Frank, M., Haley, B.A., Böniger, U., De Deckker, P., Ginge, F.X., 2011. Current transport versus continental inputs in the eastern Indian Ocean: radiogenic isotope signatures of clay size sediments. *Geochimica et Geophysica Geosystems* 12, Q06017. <http://dx.doi.org/10.1029/2011GC003544>.
- Ehlert, C., Grasse, P., Mollier-Vogel, E., Bösch, T., Franz, J., de Souza, G.F., Reynolds, B.C., Stramma, L., Frank, M., 2012. Factors controlling the silicon isotope distribution in waters and surface sediments of the Peruvian coastal upwelling. *Geochimica et Cosmochimica Acta* 99, 128–145. <http://dx.doi.org/10.1016/j.gca.2012.09.038>.
- Elderfield, H., Sholkovitz, E.R., 1987. Rare Earth Elements in the pore waters of reducing nearshore sediments. *Earth and Planetary Science Letters* 82 (3–4), 280–288. [http://dx.doi.org/10.1016/0012-821X\(87\)90202-0](http://dx.doi.org/10.1016/0012-821X(87)90202-0).
- Estrada, M., Blasco, D., 1985. Phytoplankton assemblages in coastal upwelling areas. In: Bas, C., Margalef, R., Rubies, P. (Eds.), *Simposio Internacional Sobre Las Areas de Afloramiento Mas Importantes del Oeste Africano, Cabo Blanco y Benguela*. Instituto de Investigaciones Pesqueras, Barcelona, pp. 379–402.
- Fagel, N., Hillaire-Marcel, C., Humblet, M., Bresseur, R., Weis, D., Stevenson, R.K., 2004. Nd and Pb isotope signatures of the clay-size fraction of Labrador Sea sediments during the Holocene: implications for the inception of the modern deep circulation pattern. *Paleoceanography* 19, PA3002. <http://dx.doi.org/10.1029/2003PA000993>.
- Fedorov, A.V., Philander, S.G., 2000. Is El Niño changing? *Science* 288, 1997–2002. <http://dx.doi.org/10.1126/science.288.5473.1997>.
- Feldman, G., Clark, D., Halpern, D., 1984. Satellite color observations of the phytoplankton distribution in the eastern equatorial Pacific during the 1982–1983 El Niño. *Science* 226, 1069–1071.
- Fiedler, P.C., 2002. Environmental change in the Eastern tropical Pacific Ocean: review of ENSO and decadal variability. *Marine Ecology Progress Series* 224, 265–283.
- Fiedler, P.C., Talley, L.D., 2006. Hydrography of the eastern tropical Pacific: a review. *Progress in Oceanography* 69 (2–4), 143–180. <http://dx.doi.org/10.1016/j.jpoc.2006.03.008>.
- Frank, M., 2002. Radiogenic isotopes: tracers of past ocean circulation and erosional input. *Reviews of Geophysics* 40 (1), 1001. <http://dx.doi.org/10.1029/2000RG000094>.
- Froelich, P.N., et al., 1988. Early diagenesis of organic matter in Peru continental margin sediments: phosphorite precipitation. *Marine Geology* 80 (3–4), 309–343. [http://dx.doi.org/10.1016/0025-3227\(88\)90095-3](http://dx.doi.org/10.1016/0025-3227(88)90095-3).
- Fuenzalida, R., Schneider, W., Garcés-Vargas, J., Bravo, L., Lange, C.B., 2009. Vertical and horizontal extension of the oxygen minimum zone in the eastern South Pacific Ocean. *Deep-Sea Research II* 56 (16), 1027–1038. <http://dx.doi.org/10.1016/j.dsr2.2008.11.001>.
- Georg, R.B., Reynolds, B.C., Frank, M., Halliday, A.N., 2006. New sample preparation techniques for the determination of Si isotopic compositions using MC-ICPMS. *Chemical Geology* 235 (1–2), 95–104. <http://dx.doi.org/10.1016/j.chemgeo.2006.06.006>.
- Goldstein, S.L., O’Nions, R.K., Hamilton, P.J., 1984. A Sm–Nd isotopic study of atmospheric dusts and particulates from major river systems. *Earth and Planetary Science Letters* 70 (2), 221–236. [http://dx.doi.org/10.1016/0012-821X\(84\)90007-4](http://dx.doi.org/10.1016/0012-821X(84)90007-4).
- Grasse, P., Stichel, T., Stumpf, R., Stramma, L., Frank, M., 2012. The distribution of neodymium isotopes and concentrations in the Eastern Equatorial Pacific: water mass advection versus particle exchange. *Earth and Planetary Science Letters* 353–354, 198–207. <http://dx.doi.org/10.1016/j.epsl.2012.07.044>.
- Grousset, F.E., Biscaye, P.E., Zindler, A., Prospero, J., Chester, R., 1988. Neodymium isotopes as tracers in marine sediments and aerosols: North Atlantic. *Earth and Planetary Science Letters* 87 (4), 367–378. [http://dx.doi.org/10.1016/0012-821X\(88\)90001-5](http://dx.doi.org/10.1016/0012-821X(88)90001-5).
- Gutiérrez, D., et al., 2009. Rapid reorganization in ocean biogeochemistry off Peru towards the end of the Little Ice Age. *Biogeosciences* 6, 835–848.
- Gutjahr, M., Frank, M., Stirling, C.H., Keigwin, L.D., Halliday, A.N., 2008. Tracing the Nd isotope evolution of North Atlantic Deep and intermediate waters in the

- western North Atlantic since the Last Glacial Maximum from Blake Ridge sediments. *Earth and Planetary Science Letters* 266 (1–2), 61–77. <http://dx.doi.org/10.1016/j.epsl.2007.10.037>.
- Gutjahr, M., Frank, M., Stirling, C.H., Klemm, V., van de Flierdt, T., Halliday, A.N., 2007. Reliable extraction of a deepwater trace metal isotope signal from Fe–Mn oxyhydroxide coatings of marine sediments. *Chemical Geology* 242 (3–4), 351–370. <http://dx.doi.org/10.1016/j.chemgeo.2007.03.021>.
- Haley, B.A., Klinkhammer, G.P., McManus, J., 2004. Rare Earth Elements in pore waters of marine sediments. *Geochimica et Cosmochimica Acta* 68 (6), 1265–1279. <http://dx.doi.org/10.1016/j.gca.2003.09.012>.
- Hansen, H.P., Koroleff, F., 1999. Determination of nutrients. In: Grasshoff, K., Kremling, K., Erhardt, M. (Eds.), *Methods of Seawater Analysis*. Wiley VCH, pp. 159–228.
- Haug, G.H., Hughen, K.A., Sigman, D.M., Peterson, L.C., Röhl, U., 2001. Southward migration of the intertropical convergence zone through the Holocene. *Science* 293, 1304–1308. <http://dx.doi.org/10.1126/science.1059725>.
- Higginson, M.J., Altabet, M.A., 2004. Initial test of the silicic acid leakage hypothesis using sedimentary biomarkers. *Geophysical Research Letters* 31, L18303. <http://dx.doi.org/10.1029/2004GL020511>.
- Horwitz, E.P., Chiarizia, R., Dietz, M.L., 1992. A novel strontium-selective extraction chromatographic resin. *Solvent Extraction and Ion Exchange* 10 (2), 313–336. <http://dx.doi.org/10.1080/07366299208918107>.
- Hutchins, D.A., et al., 2002. Phytoplankton iron limitation in the Humboldt Current and Peru Upwelling. *Limnology and Oceanography* 47 (4), 997–1011.
- Huyer, A., Smith, R.L., Paluszkievicz, T., 1987. Coastal upwelling off Peru during normal and El Niño times, 1981–1984. *Journal of Geophysical Research* 92 (C13), 297–307.
- Ingall, E., Jahnke, R., 1994. Evidence for enhanced phosphorus regeneration from marine sediments overlain by oxygen depleted waters. *Geochimica et Cosmochimica Acta* 58 (11), 2571–2575. [http://dx.doi.org/10.1016/0016-7037\(94\)90033-7](http://dx.doi.org/10.1016/0016-7037(94)90033-7).
- Karstensen, J., Stramma, L., Visbeck, M., 2008. Oxygen minimum zones in the eastern tropical Atlantic and Pacific oceans. *Progress in Oceanography* 77 (4), 331–350. <http://dx.doi.org/10.1016/j.pcean.2007.05.009>.
- Kessler, W.S., 2006. The circulation of the eastern tropical Pacific: a review. *Progress in Oceanography* 69, 181–217. <http://dx.doi.org/10.1016/j.pcean.2006.03.009>.
- Klevenz, V., Vance, D., Schmidt, D.N., Mezger, K., 2008. Neodymium isotopes in benthic foraminifera: core-top systematics and a down-core record from the neogene South Atlantic. *Earth and Planetary Science Letters* 265 (3–4), 571–587. <http://dx.doi.org/10.1016/j.epsl.2007.10.053>.
- Koutavas, A., Joannides, S., 2012. El Niño–Southern Oscillation extrema in the Holocene and Last Glacial Maximum. *Paleoceanography* 27, PA4208. <http://dx.doi.org/10.1029/2012PA002378>.
- Lacan, F., Jeandel, C., 2001. Tracing Papua New Guinea imprint on the central Equatorial Pacific Ocean using neodymium isotopic compositions and Rare Earth Element patterns. *Earth and Planetary Science Letters* 186, 497–512.
- Lacan, F., Jeandel, C., 2005. Neodymium isotopes as a new tool for quantifying exchange fluxes at the continent–ocean interface. *Earth and Planetary Science Letters* 232 (3–4), 245–257. <http://dx.doi.org/10.1016/j.epsl.2005.01.004>.
- Leduc, G., Vidal, L., Tachikawa, K., Bard, E., 2010. Changes in Eastern Pacific ocean ventilation at intermediate depth over the last 150 kyr BP. *Earth and Planetary Science Letters* 298 (1–2), 217–228. <http://dx.doi.org/10.1016/j.epsl.2010.08.002>.
- Le Fèvre, B., Pin, C., 2005. A straightforward separation scheme for concomitant Lu–Hf and Sm–Nd isotope ratio and isotope dilution analysis. *Analytica Chimica Acta* 543 (1–2), 209–221. <http://dx.doi.org/10.1016/j.aca.2005.04.044>.
- Loubere, P., Fariduddin, M., Richaud, M., 2011. Glacial marine nutrient and carbon redistribution: evidence from the tropical ocean. *Geochemistry Geophysics Geosystems* 12, Q08013. <http://dx.doi.org/10.1029/2011GC003546>.
- Loubere, P., Richaud, M., Liu, Z., Mekik, F., 2003. Oceanic conditions in the eastern equatorial Pacific during the onset of ENSO in the Holocene. *Quaternary Research* 60 (2), 142–148. [http://dx.doi.org/10.1016/S0033-5894\(03\)00092-9](http://dx.doi.org/10.1016/S0033-5894(03)00092-9).
- Loucaides, S., Koning, E., van Cappellen, P., 2012. Effect of pressure on silica solubility of diatom frustules in the oceans: results from long-term laboratory and field incubations. *Marine Chemistry* 136–137, 1–6. <http://dx.doi.org/10.1016/j.marchem.2012.04.003>.
- Lukas, R., 1986. The termination of the equatorial undercurrent in the Eastern Pacific. *Progress in Oceanography* 16, 63–90.
- Matsumoto, K., Sarmiento, J.L., 2008. A corollary to the silicic acid leakage hypothesis. *Paleoceanography* 23, PA2203. <http://dx.doi.org/10.1029/2007PA001515>.
- McGee, D., Marcantonio, F., Lynch-Stieglitz, J., 2007. Deglacial changes in dust flux in the eastern equatorial Pacific. *Earth and Planetary Science Letters* 257 (1–2), 215–230. <http://dx.doi.org/10.1016/j.epsl.2007.02.033>.
- McManus, J., Berelson, W.M., Coale, K.H., Johnson, K.S., Kilgore, T.E., 1997. Phosphorus regeneration in continental margin sediments. *Geochimica et Cosmochimica Acta* 61 (14), 2891–2907.
- Milligan, A.J., Varela, D.E., Brzezinski, M.A., 2004. Dynamics of silicon metabolism and silicon isotopic discrimination in a marine diatom as a function of pCO<sub>2</sub>. *Limnology and Oceanography* 49 (2), 322–329.
- Molina-Cruz, A., 1977. The relation of the southern trade winds to upwelling processes during the last 75,000 years. *Quaternary Research* 8, 324–338.
- Moore, J.K., Doney, S.C., Lindsay, K., 2004. Upper ocean ecosystem dynamics and iron cycling in a global three-dimensional model. *Global Biogeochemical Cycles* 18, GB4028. <http://dx.doi.org/10.1029/2004GB002220>.
- Moore, T.C., 2008. Biogenic silica and chert in the Pacific Ocean. *Geology* 36 (12), 975–978. <http://dx.doi.org/10.1130/G25057A.1>.
- Morley, D.W., Leng, M.J., Mackay, A.W., Sloane, H.J., Rioual, P., Battarbee, R.W., 2004. Cleaning of lake sediment samples for diatom oxygen isotope analysis. *Journal of Paleolimnology* 31 (3), 391–401. <http://dx.doi.org/10.1023/B:JOP.0000021854.70714.6b>.
- Müller, P.J., Schneider, R., 1993. An automated leaching method for the determination of opal in sediments and particulate matter. *Deep-Sea Research* 140 (3), 425–444.
- Nelson, D.M., Goering, J.J., Boisseau, D.W., 1981. Consumption and regeneration of silicic acid in three coastal upwelling systems. In: Richards, F.A. (Ed.), *Coastal Upwelling*. American Geophysical Union, pp. 242–256.
- Nozaki, Y., Yamamoto, Y., 2001. Radium 228 based nitrate fluxes in the eastern Indian Ocean and the South China Sea and a silicon-induced “alkalinity pump” hypothesis. *Global Biogeochemical Cycles* 15 (3), 555–567.
- Pennington, J.T., Mahoney, K.L., Kuwahara, V.S., Kolber, D.D., Calienes, R., Chavez, F.P., 2006. Primary production in the eastern tropical Pacific: a review. *Progress in Oceanography* 69 (2–4), 285–317. <http://dx.doi.org/10.1016/j.pcean.2006.03.012>.
- Penven, P., Echevin, V., Pasapera, J., Colas, F., Tam, J., 2005. Average circulation, seasonal cycle, and mesoscale dynamics of the Peru current system: a modeling approach. *Journal of Geophysical Research* 110, C10021. <http://dx.doi.org/10.1029/2005JC002945>.
- Pichevin, L.E., Ganeshram, R.S., Reynolds, B.C., Prah, F., Pedersen, T.F., Thunell, R., McClymont, E.L., 2012. Silicic acid biogeochemistry in the Gulf of California: insights from sedimentary Si isotopes. *Paleoceanography* 27, PA2201. <http://dx.doi.org/10.1029/2011PA002237>.
- Pichevin, L.E., Reynolds, B.C., Ganeshram, R.S., Cacho, I., Pena, L.D., Keefe, K., Ellam, R.M., 2009. Enhanced carbon pump inferred from relaxation of nutrient limitation in the glacial ocean. *Nature* 459, 1114–1117. <http://dx.doi.org/10.1038/nature08101>.
- Piegras, D.J., Jacobsen, S.B., 1988. The isotopic composition of neodymium in the North Pacific. *Geochimica et Cosmochimica Acta* 52, 1373–1381.
- Piegras, D.J., Wasserburg, G.J., 1982. Isotopic composition of neodymium in waters from the drake passage. *Science* 217, 207–214.
- Ragueneau, O., et al., 2000. A review of the Si cycle in the modern ocean: recent progress and missing gaps in the application of biogenic opal as a paleo-productivity proxy. *Global and Planetary Change* 26, 317–365.
- Rein, B., Lückge, A., Reinhardt, L., Sirocko, F., Wolf, A., Dullo, W.-C., 2005. El Niño variability off Peru during the last 20,000 years. *Paleoceanography* 20, PA4003. <http://dx.doi.org/10.1029/2004PA001099>.
- Rein, B., Lückge, A., Sirocko, F., 2004. A major Holocene ENSO anomaly during the Medieval period. *Geophysical Research Letters* 31, L17211. <http://dx.doi.org/10.1029/2004GL020161>.
- Reinhardt, L., Kudrass, H.-R., Lückge, A., Wiedicke, M., Wunderlich, J., Wendt, G., 2002. High-resolution sediment echosounding off Peru: Late Quaternary depositional sequences and sedimentary structures of a current-dominated shelf. *Marine Geophysical Researches* 23, 335–351.
- Reynolds, B.C., et al., 2007. An inter-laboratory comparison of Si isotope reference materials. *Journal of Analytical Atomic Spectrometry* 22 (5), 561–568. <http://dx.doi.org/10.1039/b616755a>.
- Reynolds, B.C., Frank, M., Halliday, A.N., 2006. Silicon isotope fractionation during nutrient utilization in the North Pacific. *Earth and Planetary Science Letters* 244, 431–443. <http://dx.doi.org/10.1016/j.epsl.2006.02.002>.
- Reynolds, B.C., Frank, M., Halliday, A.N., 2008. Evidence for a major change in silicon cycling in the subarctic North Pacific at 2.73 Ma. *Paleoceanography* 23, PA4219. <http://dx.doi.org/10.1029/2007PA001563>.
- Rodbell, D.T., Seltzer, G.O., Anderson, D.M., Abbott, M.B., Enfield, D.B., Newman, J.H., 1999. An approximately 15,000-year record of El Niño-driven alluviation in southwestern Ecuador. *Science* 283, 516–520.
- Rutberg, R.L., Hemming, S.R., Goldstein, S.L., 2000. Reduced North Atlantic deep water flux to the glacial Southern Ocean inferred from neodymium isotope ratios. *Nature* 405, 935–938. <http://dx.doi.org/10.1038/35016049>.
- Sarbas, B., Nohl, U., 2009. The GEOROC database – a decade of “online geochemistry”. *Geochimica et Cosmochimica Acta* 73, A1158.
- Sarmiento, J.L., Gruber, N., Brzezinski, M.A., Dunne, J.P., 2004. High-latitude controls of thermocline nutrients and low latitude biological productivity. *Nature* 427, 56–60. <http://dx.doi.org/10.1038/nature02204.1>.
- Saukel, C., Lamy, F., Stuut, J.-B.W., Tiedemann, R., Vogt, C., 2011. Distribution and provenance of wind-blown SE Pacific surface sediments. *Marine Geology* 280, 130–142. <http://dx.doi.org/10.1016/j.margeo.2010.12.006>.
- Scheidegger, K.F., Krissek, L.A., 1982. Dispersal deposition of eolian and fluvial sediments off Peru and northern Chile. *Geological Society of America Bulletin* 93 (2), 150–162. [http://dx.doi.org/10.1130/0016-7606\(1982\)93<150](http://dx.doi.org/10.1130/0016-7606(1982)93<150).
- Scholz, F., Hensen, C., Noffke, A., Rohde, A., Liebetrau, V., Wallmann, K., 2011. Early diagenesis of redox-sensitive trace metals in the Peru upwelling area – response to ENSO-related oxygen fluctuations in the water column. *Geochimica et Cosmochimica Acta* 75 (22), 7257–7276. <http://dx.doi.org/10.1016/j.gca.2011.08.007>.
- Stichel, T., Frank, M., Rickli, J., Haley, B.A., 2012. The hafnium and neodymium isotope composition of seawater in the Atlantic sector of the Southern Ocean. *Earth and Planetary Science Letters* 317–318, 282–294. <http://dx.doi.org/10.1016/j.epsl.2011.11.025>.
- Stumpf, R., Frank, M., Schönfeld, J., Haley, B.A., 2010. Late Quaternary variability of Mediterranean outflow water from radiogenic Nd and Pb isotopes. *Quaternary Science Reviews* 29 (19–20), 2462–2472. <http://dx.doi.org/10.1016/j.quascirev.2010.06.021>.

- Stumpf, R., Frank, M., Schönfeld, J., Haley, B.A., 2011. Climatically driven changes in sediment supply on the SW Iberian shelf since the Last Glacial Maximum. *Earth and Planetary Science Letters* 312, 80–90. <http://dx.doi.org/10.1016/j.epsl.2011.10.002>.
- Sunda, W.G., Huntsman, S.A., 1995. Iron uptake and growth limitation in oceanic and coastal phytoplankton. *Marine Chemistry* 50, 189–206. [http://dx.doi.org/10.1016/0304-4203\(95\)00035-P](http://dx.doi.org/10.1016/0304-4203(95)00035-P).
- Sutton, J.N., Varela, D.E., Brzezinski, M.A., Beucher, C.P., 2013. Species-dependent silicon isotope fractionation by marine diatoms. *Geochimica et Cosmochimica Acta* 104, 300–309. <http://dx.doi.org/10.1016/j.gca.2012.10.057>.
- Tachikawa, K., Roy-Barman, M., Michard, A., Thouron, D., Yeghicheyan, D., Jeandel, C., 2004. Neodymium isotopes in the Mediterranean Sea: comparison between seawater and sediment signals. *Geochimica et Cosmochimica Acta* 68 (14), 3095–3106. <http://dx.doi.org/10.1016/j.gca.2004.01.024>.
- Takeda, S., 1998. Influence of iron availability on nutrient consumption ratio of diatoms in oceanic waters. *Nature* 393, 774–777.
- Tanaka, T., et al., 2000. JNdi-1: a neodymium isotopic reference in consistency with LaJolla neodymium. *Chemical Geology* 168, 279–281. [http://dx.doi.org/10.1016/S0009-2541\(00\)00198-4](http://dx.doi.org/10.1016/S0009-2541(00)00198-4).
- Thiede, J., Suess, E., 1983. *Coastal Upwelling: Its Sediment Record*. Plenum Publishing Corporation, New York, p. 610.
- Toggweiler, J.R., Dixon, K., Broecker, W.S., 1991. The Peru upwelling and the ventilation of the South Pacific. *Journal of Geophysical Research* 96 (C11), 20467–20497.
- Toth, L.T., Aronson, R.B., Vollmer, S.V., Hobbs, J.W., Urrego, D.H., Cheng, H., Enochs, I.C., Combsch, D.J., van Woessik, R., Macintyre, I.G., 2012. ENSO drove 2500-year collapse of eastern Pacific coral reefs. *Science* 337, 81–84. <http://dx.doi.org/10.1126/science.1221168>.
- Tréguer, P., Nelson, D.M., van Bennekom, A.J., DeMaster, D.J., Leynaert, A., Quéguiner, B., 1995. The silica balance in the world ocean: a reestimate. *Science* 268, 375–379. <http://dx.doi.org/10.1126/science.268.5209.375>.
- Tudhope, A.W., Chilcott, C.P., McCulloch, M.T., Cook, E.R., Chappell, J., Ellam, R.M., Lea, D.W., Lough, J.M., Shimmield, G.B., 2001. Variability in the El Niño–Southern oscillation through a glacial–interglacial cycle. *Science* 291, 1511–1517. <http://dx.doi.org/10.1126/science.1057969>.
- Vance, D., Burton, K.W., 1999. Neodymium isotopes in planktonic foraminifera: a record of the response of continental weathering and ocean circulation rates to climate change. *Earth and Planetary Science Letters* 173 (4), 365–379. [http://dx.doi.org/10.1016/S0012-821X\(99\)00244-7](http://dx.doi.org/10.1016/S0012-821X(99)00244-7).
- Vance, D., Scrivner, A.E., Beney, P., Staubwasser, M., Henderson, G.M., Slowey, N.C., 2004. The use of foraminifera as a record of the past neodymium isotope composition of seawater. *Paleoceanography* 19, PA2009. <http://dx.doi.org/10.1029/2003PA000957>.
- Varela, D.E., Pride, C.J., Brzezinski, M.A., 2004. Biological fractionation of silicon isotopes in Southern Ocean surface waters. *Global Biogeochemical Cycles* 18, GB1047. <http://dx.doi.org/10.1029/2003GB002140>.
- Vargas, G., Rutllant, J.A., Ortlieb, L., 2006. ENSO tropical–extratropical climate teleconnections and mechanisms for Holocene debris flows along the hyperarid coast of western South America (17°–24°S). *Earth and Planetary Science Letters* 249, 467–483. <http://dx.doi.org/10.1016/j.epsl.2006.07.022>.
- Warnock, J., Scherer, R., Loubere, P., 2007. A quantitative assessment of diatom dissolution and late Quaternary primary productivity in the Eastern Equatorial Pacific. *Deep-Sea Research II* 54, 772–783. <http://dx.doi.org/10.1016/j.dsr2.2007.01.011>.
- Wilson, D.J., Piotrowski, A.M., Galy, A., Clegg, J.A., 2013. Reactivity of neodymium carriers in deep sea sediments: implications for boundary exchange and paleoceanography. *Geochimica et Cosmochimica Acta* 109, 197–221. <http://dx.doi.org/10.1016/j.gca.2013.01.042>.
- Wolf, A., 2002. *Zeitliche Variationen im peruanischen Küstenauftrieb seit dem Letzten Glazialen Maximum – Steuerung durch globale Klimadynamik*. Dissertation. Christian-Albrechts University Kiel, p. 115.